

# The effect of helicity on the correlation time of large scale turbulent flows

Alexandre CAMERON,<sup>\*</sup> Alexandros ALEXAKIS,<sup>†</sup> and Marc-Étienne BRACHET<sup>‡</sup>

*Laboratoire de Physique Statistique, École Normale Supérieure,  
PSL Research University; Université Paris Diderot Sorbonne Paris-Cité; Sorbonne  
Universités UPMC Univ Paris 06; CNRS; 24 rue Lhomond, 75005 Paris, France*

(Dated: October 8, 2018)

Solutions of the forced Navier-Stokes equation have been conjectured to thermalize at scales larger than the forcing scale, similar to an absolute equilibrium obtained for the spectrally-truncated Euler equation. Using direct numeric simulations of Taylor-Green flows and general-periodic helical flows, we present results on the probability density function, energy spectrum, auto-correlation function and correlation time that compare the two systems. In the case of highly helical flows, we derive an analytic expression describing the correlation time for the absolute equilibrium of helical flows that is different from the  $E^{-1/2}k^{-1}$ -scaling law of weakly helical flows. This model predicts a new helicity-based scaling law for the correlation time as  $\tau(k) \sim H^{-1/2}k^{-1/2}$ . This scaling law is verified in simulations of the truncated Euler equation. In simulations of the Navier-Stokes equations the large scale modes of forced Taylor-Green symmetric flows (with zero total helicity and large separation of scales) follow the same properties as absolute equilibrium including a  $\tau(k) \sim E^{-1/2}k^{-1}$  scaling for the correlation time. General-periodic helical flows also show similarities between the two systems, however the largest scales of the forced flows deviate from the absolute equilibrium solutions.

PACS numbers: 05.20.Jj ; 47.27.-i ; 47.27.eb ; 47.27.E- ; 47.27.ek ;

## I. INTRODUCTION

Experiments and numerical studies [1, 2] are known to reproduce, up to intermittency corrections [3], the energy spectrum power law predicted by Kolmogorov's 1941 theory of turbulence [4]:  $E(k) \propto \epsilon^{2/3}k^{-5/3}$  where  $k$  and  $\epsilon$  denote the wavenumber and the energy dissipation respectively. This power law is valid in the inertial range, *i.e.* for wavenumbers satisfying  $k_f < k < k_d$  where  $k_f$  and  $k_d \sim k_f Re^{3/4}$  denote the forcing wavenumber and the viscous dissipation wavenumber respectively. The Reynolds number,  $Re$ , is defined as  $Re \equiv U/\nu k_f$  where  $U$  stands for the root mean square velocity and  $\nu$  denotes the viscosity. In order to maximize the size of this inertial range, most experiments and direct numeric simulations (DNS) forced the flow at the largest scale of the system. At these scales the dynamics of the system can be described in terms of the Richardson cascade [3] where large scales transfer their energy to smaller scales with large eddies breaking into smaller eddies. This simple description cannot be used to describe the dynamics at scales larger than the forcing scale (from now on referred to as the *large scales*). Indeed, contrary to the inertial range, large scales do not have a direct flux of energy coming from the forcing scale. Some theoretical arguments [3, 5, 6] indicate that they can be described by the dynamics of absolute equilibrium solutions of the spectrally truncated Euler equation (*TEE*) given by

$$\partial_t \mathbf{u} + \mathbb{P}_{k_M}[\mathbf{u} \cdot \nabla \mathbf{u} + \nabla P] = 0 \quad \text{and} \quad \nabla \cdot \mathbf{u} = 0, \quad (1)$$

where  $\mathbf{u}$ ,  $P$  and  $k_M$  denote the velocity field, the pressure field and the truncation wavenumber respectively. The operator  $\mathbb{P}_{k_M}$  enforces a spherical truncation in the *TEE*. It acts in Fourier space as a small scale filter. The modes whose wavenumbers satisfy  $|\mathbf{k}| \leq k_M$ , are unaffected by the projection whereas the amplitudes of the other modes are all set to zero. Despite keeping the amplitude of the truncated modes to zero, the projection conserves the total energy and helicity of the flows. After a transient state, the system reaches an absolute equilibrium state which has been conjecture to follow a Boltzmann-Gibbs distribution depending only on the initial energy and helicity of the flow. Under these assumptions, Kraichnan [7] predicted the form of the energy and helicity spectrum. DNS of the *TEE* performed in [8, 9] verified the absolute equilibrium energy and helicity spectra predicted in [7].

The *TEE* (1) needs to be contrasted with the forced Navier-Stokes equation (*NSE*) that governs the evolution of viscous flows and is given by

$$\partial_t \mathbf{u} + (\mathbf{u} \cdot \nabla) \mathbf{u} = -\nabla P + \nu \Delta \mathbf{u} + \mathbf{F} \quad \text{and} \quad \nabla \cdot \mathbf{u} = 0, \quad (2)$$

<sup>\*</sup> alexandre.cameron@ens.fr

<sup>†</sup> alexakis@lps.ens.fr

<sup>‡</sup> brachet@physique.ens.fr

where  $\mathbf{u}$ ,  $P$  and  $\nu$  denote the velocity field, the pressure field and the viscosity respectively.  $\mathbf{F}$  denotes the forcing field that is acting at a particular wavenumber  $k_f$ . Note that unlike the *TEE*, in the *NSE*, energy needs to be supplied by the forcing term, in order to compensate viscous dissipation. As result of the presence of viscosity, the solutions of the equation are dependent on the Reynolds number. Furthermore, the energy and helicity of the system at steady state are not determined by the initial conditions as in the *TEE*, but depend on the forcing, the domain size and the viscosity. Despite these differences, the large scales could, in principle, be modeled as in the state of absolute equilibrium predicted in [7] due to the absence of mean flux of energy. Recently, Dallas *et al.* [10] performed turbulent DNS with enough resolution to model flows with significant scale separation between the forcing scale  $\ell_f \propto 1/k_f$  and the domain scale  $L$ . In their study, it was reported that large scale spectra are in agreement with the absolute equilibrium theory, although some deviations at scales the order of the domain size were reported. Among other reasons, these deviations could be attributed to large scale instabilities [11, 12].

Agreement in the spectra however does not guarantee the presence of an absolute equilibrium, since the temporal dynamics can be different. The differences (or the equivalence) between the temporal dynamic of the large scale modes of solution of the *NSE* and the absolute equilibrium solutions of the *TEE* have not yet been investigated. Note that the equivalence of the temporal dynamic of the two systems is a much more stringent condition than the simple equivalence of their spatial spectra. The correlation time of the system is a good measurement to asses the temporal dynamic of large scale modes. In pseudo-spectral DNS, the Eulerian correlation time of the modes of the velocity field is the best suited to describe the temporal dynamic of the system. Numerical solutions have already been used to analyze the temporal evolution of statistical equilibrium in the statistically stationary regime without helicity in [8] and in the transitory regime with helicity in [9]. But the characterization of the correlation time and comparison with the large scales of the *NSE* has not yet been performed.

The aim of the present paper is to compare the statistics of individual modes and the temporal properties of the *TEE* solutions and those of the large scales of the *NSE*. In the next section II we review absolute equilibrium theory and derive analytic results for the correlation time of incompressible flows solutions of the *TEE* for arbitrary helicity. In section III we validate these predictions with numerical solutions of the *TEE* while in section IV we test if they also apply to the large scales of solutions of the *NSE* for different forcing functions. Our conclusions are drawn in the last section.

## II. ABSOLUTE EQUILIBRIUM AND THERMALIZATION THEORY

### A. Energy and helicity spectra

The derivation of absolute equilibrium statistics for helical flows was carried out by Kraichnan [7, 13] in an analogy to micro-canonical ensembles in statistical thermodynamics [14]. Similarly to the micro-canonical ensemble, the *TEE* conserves the total energy,  $E$ . In addition, the *TEE* also conserves the total helicity,  $H$ , which is another global quadratic quantity in velocity

$$E = \frac{1}{2} \frac{1}{L^3} \int |\mathbf{u}|^2 d\mathbf{r} \quad \text{and} \quad H = \frac{1}{2} \frac{1}{L^3} \int \mathbf{u} \cdot \boldsymbol{\omega} d\mathbf{r}, \quad (3)$$

where  $L^3 = \int d\mathbf{r}$  and  $\boldsymbol{\omega} = \nabla \times \mathbf{u}$ .

In analogy with the thermodynamic canonical ensemble, in a statistically steady state, absolute equilibrium solutions of the *TEE* will correspond to a flow in a state  $\mathbf{u}$  with probability  $\mathcal{P}(\mathbf{u})$  that follows the Boltzmann-Gibbs distribution

$$\mathcal{P}(\mathbf{u}) = \frac{1}{Z} e^{-\mathcal{C}(\mathbf{u})}. \quad (4)$$

The functional  $\mathcal{C}(\mathbf{u})$  is a linear combination of the energy  $E$  and the helicity  $H$  of the flow

$$\mathcal{C}(\mathbf{u}) = \alpha E + \beta H = \alpha \left( E - \mathcal{K}r \frac{H}{k_M} \right) \quad \text{and} \quad \mathcal{K}r = -\frac{\beta k_M}{\alpha} \quad (5)$$

where  $\alpha$  and  $\beta$  are two parameters introduced by Kraichnan. These parameters unequivocally define a class of absolute equilibrium solutions of the *TEE* with a fixed energy  $E$  and helicity  $H$ . What we presently call the Kraichnan number:  $\mathcal{K}r$  is a dimensionless combination of  $\alpha$ ,  $\beta$  and  $k_M$ . The Kraichnan number indicates the degree of helicity of the flow. When  $\mathcal{K}r=0$ , the flow does not have helicity, whereas when  $|\mathcal{K}r| = 1$  the flow is maximally helical. As of consequence of the definition of  $\mathcal{C}(\mathbf{u})$ , velocity modes are independent Gaussian variables. The partition function  $Z$  used as normalization in eq. (4) is defined by

$$Z = \int \mathcal{D}\mathbf{u} e^{-\mathcal{C}(\mathbf{u})}. \quad (6)$$

Similarly to statistical thermodynamics, Boltzmann-Gibbs weights can be used to compute statistical averages over the space of incompressible flows. The average of a generic observable  $f(\mathbf{u})$  is then given by

$$\langle f(\mathbf{u}) \rangle = \frac{1}{Z} \int \mathcal{D}\mathbf{u} f(\mathbf{u}) e^{-C(\mathbf{u})} \quad (7)$$

In the case of the *TEE*, the truncation in wavenumber implies that the functional integral can be done over a finite number of Fourier modes  $\tilde{\mathbf{u}}_{\mathbf{k}}$  that satisfy the incompressibility condition  $\mathbf{k} \cdot \tilde{\mathbf{u}}_{\mathbf{k}} = 0$ . This last condition can be simplified by using the Craya-Herring [15, 16] helical decomposition. Each Fourier mode  $\tilde{\mathbf{u}}_{\mathbf{k}}$  is written as the sum of two modes of opposite helicity:  $\tilde{\mathbf{u}}_{\mathbf{k}} = \tilde{\mathbf{u}}_{\mathbf{k}}^+ + \tilde{\mathbf{u}}_{\mathbf{k}}^-$ , where

$$\tilde{\mathbf{u}}_{\mathbf{k}}^{\pm} = \frac{1}{2} \left[ \tilde{\mathbf{u}}_{\mathbf{k}} \pm \frac{\tilde{\boldsymbol{\omega}}_{\mathbf{k}}}{k} \right] \quad (8)$$

with  $\tilde{\boldsymbol{\omega}}_{\mathbf{k}} = i\mathbf{k} \times \tilde{\mathbf{u}}_{\mathbf{k}}$ . This leads to two independent complex amplitudes  $\tilde{\mathbf{u}}_{\mathbf{k}}^{\pm}$  for each Fourier mode of an incompressible flow. Using this statistical average of eq. (7), the average energy and helicity of the modes of the flow can be derived analytically. Since the PDF of every mode of the velocity field follows a Gaussian distribution, the average energy  $\langle e_{\mathbf{k}} \rangle = \frac{1}{2} \langle |\tilde{\mathbf{u}}_{\mathbf{k}}|^2 \rangle$  and average helicity  $\langle h_{\mathbf{k}} \rangle = \frac{1}{2} \langle \tilde{\mathbf{u}}_{-\mathbf{k}} \cdot \tilde{\boldsymbol{\omega}}_{\mathbf{k}} \rangle$  of each wavevector are given by

$$\langle e_{\mathbf{k}} \rangle = \frac{\alpha^{-1}}{1 - \left( \mathcal{K}r \frac{k}{k_M} \right)^2} \quad \text{and} \quad \langle h_{\mathbf{k}} \rangle = \frac{\beta}{\alpha} \frac{\alpha^{-1} k^2}{1 - \left( \mathcal{K}r \frac{k}{k_M} \right)^2} = \frac{\beta}{\alpha} k^2 \langle e_{\mathbf{k}} \rangle. \quad (9)$$

When  $|\mathcal{K}r| \rightarrow 1$ , the energy is confined in the modes in the smallest scales of wavenumber near  $k_M$ .

The absolute equilibrium distribution can be expressed using the Craya-Herring [15, 16] helical decomposition for the energies  $\langle e_{\mathbf{k}}^{\pm} \rangle = \frac{1}{2} \langle |\tilde{\mathbf{u}}_{\mathbf{k}}^{\pm}|^2 \rangle$  and helicities  $\langle h_{\mathbf{k}}^{\pm} \rangle = \pm k \langle e_{\mathbf{k}}^{\pm} \rangle$

$$\langle e_{\mathbf{k}}^{\pm} \rangle = \frac{1}{2} \frac{\alpha^{-1}}{1 - (\pm) \mathcal{K}r \frac{k}{k_M}} \quad \text{and} \quad \langle h_{\mathbf{k}}^{\pm} \rangle = \frac{1}{2} \frac{\pm \alpha^{-1} k}{1 - (\pm) \mathcal{K}r \frac{k}{k_M}}. \quad (10)$$

When  $\mathcal{K}r \rightarrow 1$ , the energy is confined in the small scale modes and more precisely in their positive helical component. The energy spectra are then obtained by spherically averaging over all modes of the same modulus

$$E^{\pm}(k) \equiv \sum_{|\mathbf{k}|=k} \langle e_{\mathbf{k}}^{\pm} \rangle \simeq \frac{2\pi k^2 \alpha^{-1}}{1 - (\pm) \mathcal{K}r \frac{k}{k_M}} \quad \text{and} \quad E(k) = E^+(k) + E^-(k) \simeq \frac{4\pi k^2 \alpha^{-1}}{1 - \left( \mathcal{K}r \frac{k}{k_M} \right)^2} \quad (11)$$

and similarly for the helicity spectra

$$H^{\pm}(k) \equiv \sum_{|\mathbf{k}|=k} \langle h_{\mathbf{k}}^{\pm} \rangle \simeq \frac{\pm 2\pi k^3 \alpha^{-1}}{1 - (\pm) \mathcal{K}r \frac{k}{k_M}} \quad \text{and} \quad H(k) = H^+(k) + H^-(k) \simeq \frac{4\pi k^4 \alpha^{-2} \beta}{1 - \left( \mathcal{K}r \frac{k}{k_M} \right)^2}. \quad (12)$$

## B. Correlation times of absolute equilibrium solutions

The derivations so far predict the ensemble average of the energy and helicity per mode. However they do not characterize the temporal properties of the system. The computation of the spectra only requires the knowledge of the conserved quantities of the *TEE* and not the equation itself. To describe with more depth the properties of the solutions of the *TEE* or the *NSE* in the thermalization domain, the temporal properties of the flows must be analyzed.

In [8], Cichowlas *et al.* studied the correlation time of absolute equilibrium solutions of the *TEE* without helicity. It was shown that the correlation time  $\tau_{\mathbf{k}}^E$  (defined more precisely below: eq. (17)) depends on the energy  $E$  of the flow and is inversely proportional to the wavenumber  $\mathbf{k}$

$$\tau_{\mathbf{k}}^E \propto k^{-1} E^{-1/2}. \quad (13)$$

In this present work, we extend this result for flows with an arbitrary helicity and show that a new power law emerges when the flow is strongly helical. This new power law depends on the helicity  $H$  of the flow rather than the energy and reads

$$\tau_{\mathbf{k}}^H \propto k^{-1/2} H^{-1/2}. \quad (14)$$

This new power law is valid for highly helical flows and wavenumbers in the range  $k_c \ll k \ll k_M$  where  $k_c \propto k_M(1 - |\mathcal{K}r|) \ln(1 - |\mathcal{K}r|)$ , while the non-helical scaling law of eq. (13) is valid for  $k \ll k_c$ . In what follows, we give a sketch of the derivation of eq. (13) and (14) while the full derivation is presented in appx. VI.

The correlation time will be built using the short time approximation of the correlation function. The temporal correlation function  $\Gamma_{\mathbf{k}}(t)$  of a mode is defined as

$$\Gamma_{\mathbf{k}}(t) = \frac{\overline{\mathbf{u}_{\mathbf{k}}^*(s)\mathbf{u}_{\mathbf{k}}(s+t)}}{\overline{|\mathbf{u}_{\mathbf{k}}(s)|^2}} \quad \text{where} \quad \overline{f(s)} = \lim_{T \rightarrow \infty} \frac{1}{2T} \int_{-T}^T f(s) ds. \quad (15)$$

It satisfies the relations  $\Gamma_{\mathbf{k}}(0) = 1$  and  $\Gamma_{\mathbf{k}}(t) = \Gamma_{\mathbf{k}}(-t)$ . If the system loses memory as time elapses, the correlation function also satisfies  $\Gamma_{\mathbf{k}}(\infty) = 0$ . Thus, the correlation function assesses how fast a mode de-correlates from its initial value. Using the Taylor expansion of the correlation function near  $t = 0$ , the correlation function can be written as

$$\Gamma_{\mathbf{k}}(t) = 1 - \frac{1}{2}t^2\tau_{\mathbf{k}}^{-2} + \dots \quad \text{with} \quad \tau_{\mathbf{k}}^{-2} = -\partial_t^2 \Gamma_{\mathbf{k}}|_{t=0} = -\frac{\overline{\mathbf{u}_{\mathbf{k}}^*(s)\partial_t^2 \mathbf{u}_{\mathbf{k}}(s+t)}|_{t=0}}{\overline{|\mathbf{u}_{\mathbf{k}}(s)|^2}}, \quad (16)$$

where  $\tau_{\mathbf{k}}$  will be referred to as the parabolic correlation time. The term  $-\overline{\mathbf{u}_{\mathbf{k}}^*(s)\partial_t^2 \mathbf{u}_{\mathbf{k}}(s+t)}|_{t=0}$  can be rewritten as  $|\partial_t \mathbf{u}_{\mathbf{k}}(s+t)|_{t=0}^2$  using an integration by parts. Assuming that the *TEE* system is ergodic, the averages over time can be replaced by the statistical averages defined in eq. (7). The correlation time can then be expressed as

$$\tau_{\mathbf{k}} = \sqrt{\frac{\langle |\mathbf{u}_{\mathbf{k}}|^2 \rangle}{\langle |\partial_t \mathbf{u}_{\mathbf{k}}|^2 \rangle}}. \quad (17)$$

The expression of  $\langle |\mathbf{u}_{\mathbf{k}}|^2 \rangle$  is given by the absolute equilibrium statistics. On the other hand, the expression of  $\langle |\partial_t \mathbf{u}_{\mathbf{k}}|^2 \rangle$  can be computed using the temporal evolution equation of the mode given by eq. (1) in the case of the *TEE*. The property that the modes of the velocity field are independent Gaussian variables is used to compute the averages.

In the limit where  $\mathcal{K}r \rightarrow 1$  and  $k/k_M \rightarrow 0$ , it is possible to compute an asymptotic expression of the correlation time with the Craya-Herring helical decomposition [15, 16] (see appx. VI). In this limit, most of the energy is concentrated in the positive helical components of the modes near  $k_M$ . The interactions of these modes are the dominant terms in the temporal evolution equation and give a theoretical prediction for the correlation time

$$\tau_{\mathbf{k}} \simeq \sqrt{\frac{\langle |\mathbf{u}_{\mathbf{k}}^+|^2 \rangle}{\langle |\partial_t \mathbf{u}_{\mathbf{k}}^+|^2 \rangle}} \Big|_{\substack{\mathcal{K}r \rightarrow 1 \\ k/k_M \rightarrow 0}} = \sqrt{\frac{\frac{15}{8}(1 - \mathcal{K}r) - \frac{k}{k_M \ln(1 - \mathcal{K}r)}}{4\pi\alpha^{-1}k^2(1 - s_{\mathbf{k}}\mathcal{K}r\frac{k}{k_M})}} \quad \text{with} \quad \alpha = \frac{\tanh^{-1}(\mathcal{K}r) - \mathcal{K}r}{2E_{tot}\mathcal{K}r^3}. \quad (18)$$

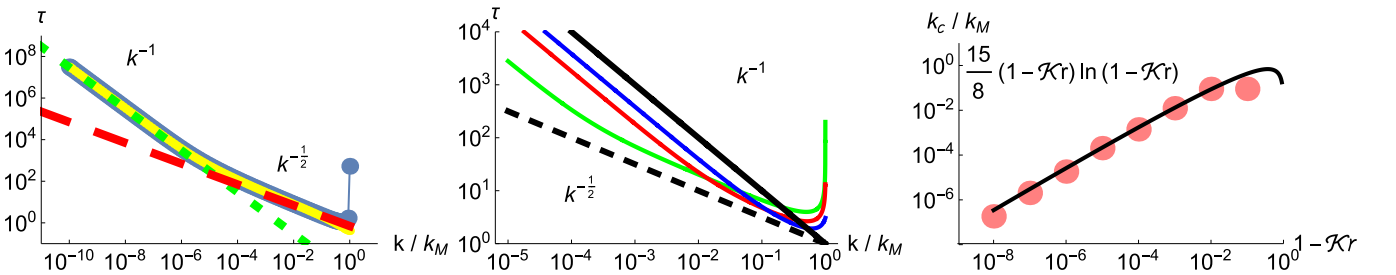


Figure 1: Left) Correlation time as a function of the wavenumber for  $1 - \mathcal{K}r = 10^{-6}$ . The results are represented with the full line with dark dots for the positive helical components and in bright dots for the negative helical components. The  $k^{-1/2}$ -scaling law is represented with the dashed line. The  $k^{-1}$ -scaling law is represented with the dotted line. Center) Dependence of the correlation time for the positive helical component. The Kraichnan number is increased at fixed energy:  $\mathcal{K}r \in \{1 - 10^{-1}; 1 - 10^{-2}; 1 - 10^{-4}\}$ , represented by blue, red and green lines respectively. The dotted line represents the  $k^{-1/2}$ -scaling law and the full line represents the  $k^{-1}$ -scaling law. Right) Transition wavenumber as a function of  $1 - \mathcal{K}r$ , the semi-analytic prediction is represented with dots and the  $\frac{15}{8}(1 - \mathcal{K}r) \ln(1 - \mathcal{K}r)$  scaling law is represented with the full line.

The left panel of fig. 1 represents the correlation time  $\tau_{\mathbf{k}}$  as a function of  $k$  for a Kraichnan number near one:  $\mathcal{K}r = 1 - 10^{-6}$ . Both power laws  $k^{-1}$  and  $k^{-1/2}$  are represented. The  $k^{-1}$ -power law is valid in the largest wavenumbers:  $k \ll k_c$ , while the  $k^{-1/2}$ -power law is valid for an intermediate range of wavenumber:  $k_c \ll k \ll k_M$ . The center panel

of fig. 1 represents the dependence of the correlation time at different Kraichnan numbers for fixed total energy  $E_{tot}$ . As  $\mathcal{K}r \rightarrow 1$ , the correlation time in the small scales increases and the correlation time in the large scales decreases. For absolute equilibrium solutions of the  $TEE$ , increasing the helicity slows down the dynamic of the small scales and makes the dynamic of the large scales more rapid. The right panel of fig. 1 represents the dependence of the transition wavenumber  $k_c$  with  $1 - \mathcal{K}r$ . The value of the transition wavenumber was estimated using the intersection of the two power laws. The dark curve on the graph indicates that the critical wavenumber follows closely the  $A(1 - \mathcal{K}r) \ln(1 - \mathcal{K}r)$  prediction. Even though the helicity does not appear explicitly in eq. (18), the correlation time has a  $k^{-\frac{1}{2}}$ -scaling for intermediate wavenumbers when  $1 - \mathcal{K}r \ll k/k_M \ll 1$ . This scaling is similar to the helicity-based correlation time (see eq. (14)) and appears for a range of Kraichnan numbers corresponding to highly helical flows.

### III. TRUNCATED EULER DNS

In the previous section, we discussed some predictions on the properties of the PDF, the standard derivation and the correlation time of solutions of the  $TEE$ . We will now check their validity in periodic flows with and without  $TG$  symmetries [17]. The DNS with  $TG$  symmetries are performed using the pseudo-spectral code TYGRES [18] and those without  $TG$  symmetries were performed using the pseudo-spectral code GHOST [19, 20]. The major advantage of studying flows with  $TG$  symmetries is that the symmetries can be used to gain a factor 32 both in storage and execution time. However, flows with  $TG$  symmetries have a total helicity equal to zero and consequently always have a Kraichnan number equal to zero. In order to study helical flows, DNS have to be performed in the general-periodic domain without  $TG$  symmetry. This last configuration will be referred to as general-periodic flow in opposition to  $TG$  symmetric flows.

#### A. No helicity: inviscid Taylor-Green flows

The first flows used to probe the statistical properties of the  $TEE$  have  $TG$  symmetries that impose the total helicity to be equal to zero. As a consequence of  $TG$  symmetries [21], the Fourier expansion of the flow can be expressed with the following simplified expression

$$\begin{bmatrix} u_r^x \\ u_r^y \\ u_r^z \end{bmatrix} = \sum_{k_x=0}^{\infty} \sum_{k_y=0}^{\infty} \sum_{k_z=0}^{\infty} \begin{bmatrix} u_{\mathbf{k}}^x \times \sin k_x x \cos k_y y \cos k_z z \\ u_{\mathbf{k}}^y \times \cos k_x x \sin k_y y \cos k_z z \\ u_{\mathbf{k}}^z \times \cos k_x x \cos k_y y \sin k_z z \end{bmatrix}, \quad (19)$$

where  $\mathbf{u}_{\mathbf{k}} \in \mathbb{R}^3$  if  $k_x, k_y, k_z$  are all odd or all even integers and  $\mathbf{u}_{\mathbf{k}} = 0$  otherwise. All the properties of the Fourier coefficients related to  $TG$  symmetries can be found in the appendix of [21]. Specific properties useful to understand the number of independent variables of  $TG$  symmetric flows are presented in appx.VII.

Incompressible random flows with  $TG$  symmetries and energy equipartition were used to initialize the simulations. Since  $TG$  symmetric flow do not have helicity ( $H = 0$  and  $\mathcal{K}r = 0$ ), the thermalization theory of Sect. IIB predicts that they should follow

$$\langle e_{\mathbf{k}} \rangle = \alpha^{-1} \quad \text{thus} \quad E(k) = \frac{4\pi k^2}{k_M^3} \alpha^{-1} \quad \text{and} \quad \tau_{\mathbf{k}} \underset{k/k_M \rightarrow 0}{=} \sqrt{\frac{45\alpha}{112}} \frac{1}{k}. \quad (20)$$

The first hypothesis in the absolute equilibrium theory is that the components of velocity are independent Gaussian variables. As detailed in appx.VII, in  $TG$  flows, the even modes with one of their components equal to zero – *i.e.* of the form  $(0, k_y, k_z)$ ,  $(k_x, 0, k_z)$  or  $(k_x, k_y, 0)$  – and the  $xy$ -diagonal modes – *i.e.* of the form  $(k_{\perp}, k_{\perp}, k_{\parallel})$  – both only have one degree of freedom corresponding to their real amplitude. All other  $TG$  modes have two degrees of freedom. To test this assumption, temporal series of the modes are recorded and analyzed to extract the PDF. PDFs of modes with one degree of freedom are presented in the left panel of the fig. 2 at different wavenumbers. On the semi-logarithmic scale, the distributions of the modes follow the parabolic trend characteristic of Gaussian distribution. The right panel of fig. 2 represents the distribution of energy of the different velocity modes. By definition, the energy is the sum of the square of the velocity components. If at a particular wave number  $\mathbf{k}$  there are  $g$  modes that are independent and Gaussian then the distribution of the energy  $e_{\mathbf{k}}$  that lies at that wavenumber must follow a  $\chi_g^2$ -distribution [22]

$$\chi_g^2(e_{\mathbf{k}}) = \frac{1}{2^{\frac{g}{2}} \Gamma(\frac{g}{2})} (e_{\mathbf{k}})^{\frac{g}{2}-1} \exp\left[-\frac{e_{\mathbf{k}}}{2}\right]. \quad (21)$$

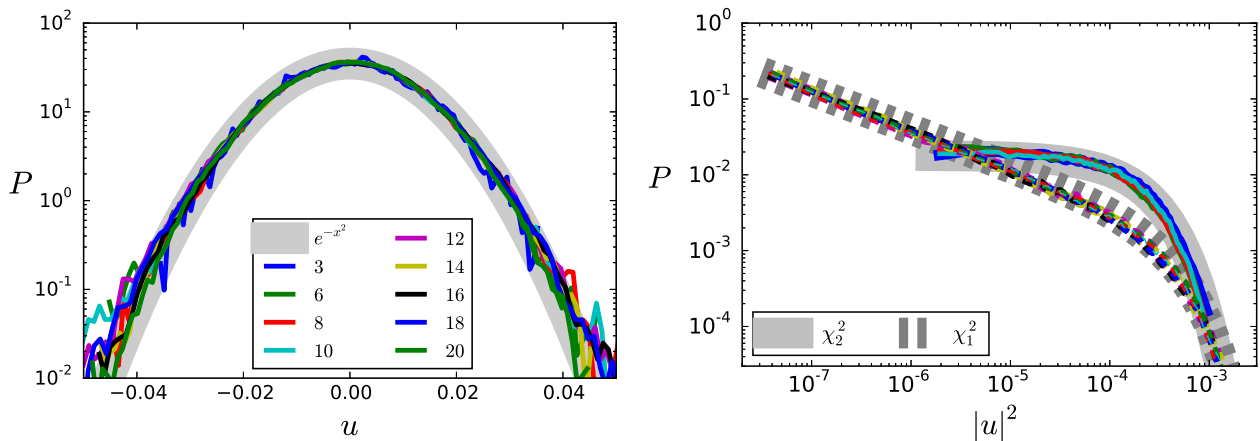


Figure 2: Left) PDF of the amplitude of the velocity of modes with one degree of freedom of Taylor-Green symmetric DNS in semi-logarithmic scale. Right) PDF of energy of the modes of Taylor-Green symmetric DNS of the truncated Euler equation in logarithmic scale: (thick) theoretical predictions, (thin dashed) one degree of freedom, (thin full) two degrees of freedom.

where  $g$  denotes the number of independent Gaussian variables (see appx.VIII). Thus, the power-law behavior at small values of  $e_{\mathbf{k}}$  reveals the degrees of freedom involved. Due to the symmetries of the *TG* flows different wavenumbers have different degrees of freedom. The modes  $-(0, k_y, k_z), (k_x, 0, k_z), (k_x, k_y, 0)$  and  $(k_{\perp}, k_{\perp}, k_{\parallel})$  – have one degree of freedom and should have an energy distribution following a  $\chi_1^2$ -law. All other modes have two degrees of freedom and have an energy distribution following a  $\chi_2^2$ -law. If the energy follows a  $\chi^2$ -distribution, it does not necessarily imply that the velocity has a Gaussian statistics, it is only a characteristic of the sum of Gaussian distributions. However, we will only check the Gaussian statistics of modes with one degree of freedom and look at the energy distribution of the other modes.

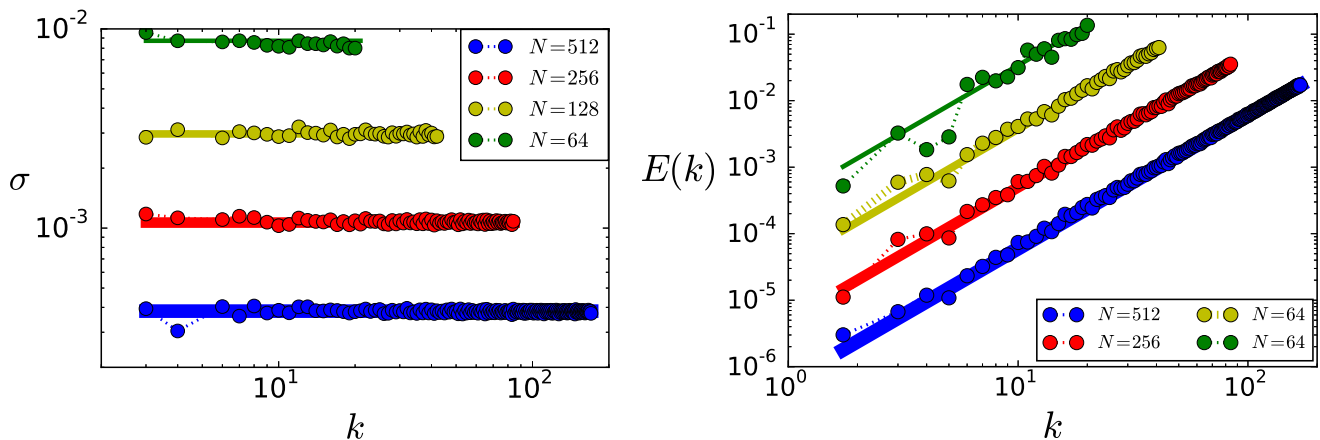


Figure 3: Left) Average standard deviation of the velocity of Taylor-Green symmetric DNS of the truncated Euler equation for different resolutions. Right) Energy spectrum of Taylor-Green symmetric DNS of the truncated Euler equation at different resolutions  $N = \{64, 128, 256, 512\}$  for a fixed energy.

To check the equipartition of the energy, the standard deviation of modes can be computed with their temporal series or the energy of all the modes within a shell of constant wavenumbers can be summed. The first method can be performed with the temporal series used to plot the PDF of the modes in fig. 2. Using this time average, the standard deviation,  $\sigma^2 = \langle e_{\mathbf{k}} \rangle$ , is represented in the left panel of fig. 3. The second method, with the shell-summed energy at a fixed time, is presented in the right panel of fig. 3. If the system satisfies energy equipartition and is ergodic, the amount of energy per shell should be proportional to the surface of the shell,  $4\pi k^2$ . The  $k^2$ -power law followed by the energy spectrum in the right panel of fig. 3 is therefore consistent with the equipartition of energy and ergodicity.

### 1. Correlation time computation

The temporal statistics of the modes depend on the evolution equation and not only on the conserved quantities. Since the correlation function and consequently the correlation time are specific properties of the evolution equation, their measurement characterizes the temporal evolution of the system. In order to compute the correlation function and assess the correlation time, we developed a method similar to that used to produce spatio-temporal spectrum in wave experiments [23–25], where the spatio-spectral spectrum  $S(k, \omega)$  is first calculated and the correlation function  $\Gamma(k, t)$  is obtained by a Fourier transform using the Wiener-Khinchin theorem [26]. This method is explained in appx. IX. Fig. 4 presents in the left panel the spatio-temporal color-plot of the power spectrum  $S(k, \omega)$  and in the right panel the correlation function  $\Gamma(k, t)$ .

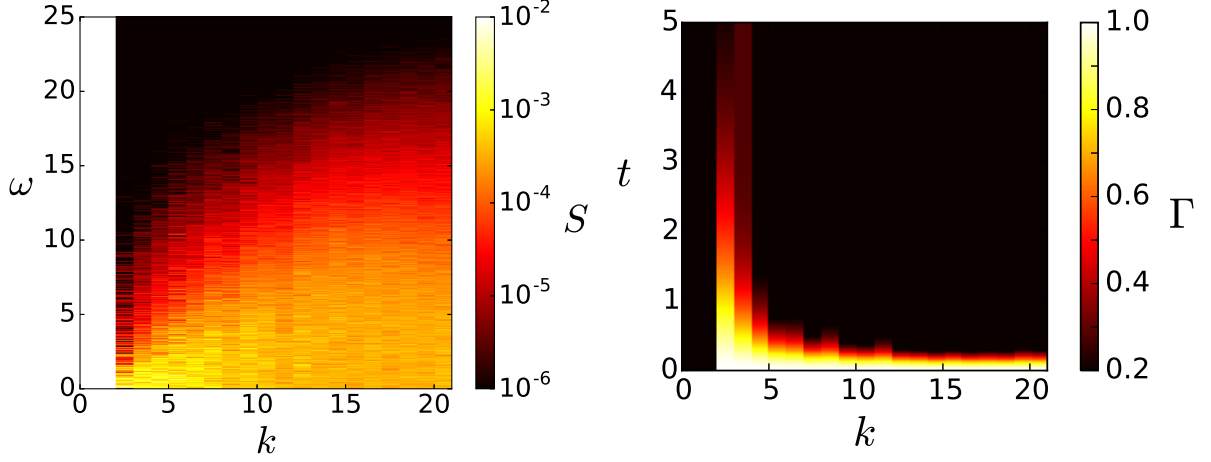


Figure 4: Spatio-temporal spectrum of Taylor-Green symmetric DNS of the truncated Euler equation. The numeric data is represented with dots and the theoretical prediction with full lines. Left) Power spectrum  $S(k, \omega)$ . Right) Correlation function  $\Gamma(k, t)$ .

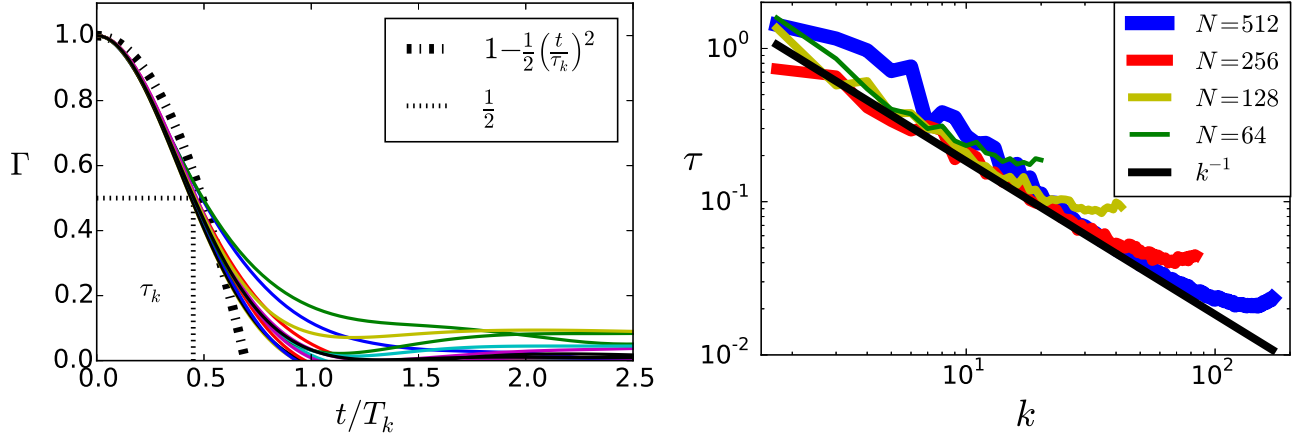


Figure 5: Temporal correlation properties of Taylor-Green symmetric DNS of the truncated Euler equation. Left) Correlation function as a function of time. Right) Correlation time as a function of wavenumber. The  $k^{-1}$ -power law is plotted with the normalization deriving from eq. (20).

The correlation functions for different velocity modes are shown in the left panel of fig. 5. The time of each correlation function has been re-scaled by the correlation time measured. As shown in the left panel of fig. 5, the correlation functions collapse on the same curve for times in the range  $0 \leq t \leq \tau_k$ . Since long time-series are required for the correlation function to converge at long times, the curves only collapse for  $t < \tau_k$ . This collapse at small time confirms that the parabolic assumption made in eq. (17) is valid for absolute equilibrium solutions of the *TEE*. Furthermore, the good agreement of the curve until  $\tau_k$  also confirms that the half-height time is a good proxy to

measure the correlation time. The right panel of fig. 5 represents the correlation time of an absolute equilibrium solution of the *TEE*. It shows that the correlation time follows a  $k^{-1}$ -scaling law characteristic of an energy-based correlation time. The thermodynamic model developed in the previous section is therefore in excellent agreement with the measurements carried out with *TG* symmetric DNS.

### B. Inviscid flows with helicity

The next set of DNS of the *TEE* were carried out using the pseudo-spectral code GHOST [19, 20]. In these DNS, for every wavenumber four real degrees of freedom exist. Indeed, the Craya-Herring helical decomposition [15, 16] states that every Fourier mode of velocity can be separated into a positive and a negative helical component as expressed in eq. (10). The two helical components are modulated by their complex amplitude. Since there is no additional restriction on the amplitude of the mode, the velocity modes have four real degrees of freedom.

All flows are initialized with the same energy, but different helicity which determines the Kraichnan number  $\mathcal{K}r = -k_M\beta/\alpha$ . This parameter is not present for the *TG* flows and leads to major differences in the global aspect of the PDF of the modes. For the same wavenumber, the helical components of helical flows have different energies.

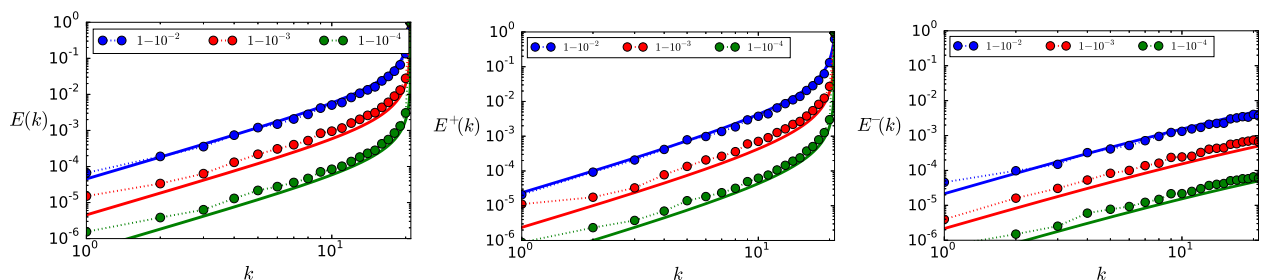


Figure 6: Energy spectrum for different Kraichnan numbers  $\mathcal{K}r \in \{1 - 10^{-2}; 1 - 10^{-3}; 1 - 10^{-4}\}$  for general-periodic solutions of the truncated Euler equation. The numeric data is represented with dots and the theoretical prediction with full lines. Left) Energy spectrum associated to the total velocity. Center) Energy spectrum associated to the positive helical component of the velocity. Right) Energy spectrum associated to the negative helical component of the velocity. On both panels, the full lines are associated with the energy of the total velocity; the dotted lines are associated with the energy of the positive helical component of the velocity; and the dashed lines are associated with the energy of the negative helical component of velocity.

Fig. 6 represents the energy spectrum of the highly helical flows  $\mathcal{K}r = \{1 - 10^{-2}; 1 - 10^{-3}; 1 - 10^{-4}\}$ . The results in the left panel come from DNS and those in the right panel are from the absolute equilibrium theory [7]. Theoretical and numerical results match, which confirms the validity of absolute equilibrium theory.

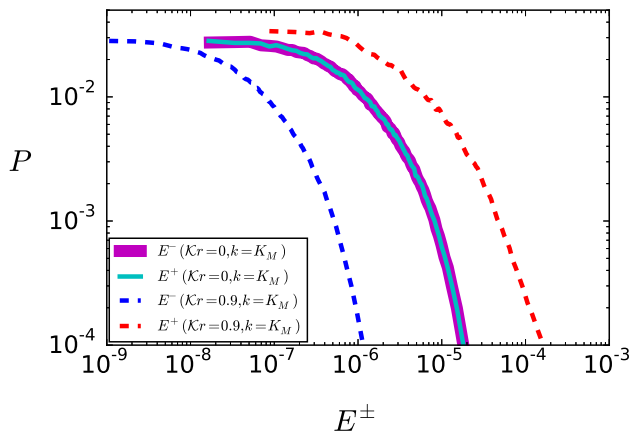


Figure 7: Separation of the PDFs due to helicity in solutions of the truncated Euler equation. The PDFs have been rescaled to plateau at the same level near zero in order to compare the width of the tail of the distribution at large values. At  $k = k_M$ , the distributions of probability have an off-set for  $\mathcal{K}r = 0.9$  because helicity greatly affects the distribution of energy in the small scales.



Fig. 7 presents the PDF of the helical components of the velocity of two general-periodic flows with different Kraichnan numbers. The first flow has a Kraichnan number of zero and consequently does not have any helicity. The second flow has a Kraichnan number of 0.9 and is thus highly helical. For every wavenumber and every Kraichnan number, the energy of the positive and negative helical components of the velocity follow a  $\chi_2^2$ -distribution. The  $\chi_2^2$ -distribution is characteristic of the sum of the square of two independent Gaussian variables. The hypothesis of Gaussian-distributed velocity modes is therefore in agreement with the DNS. The PDFs of the positive and negative helical modes at  $k = k_M$  collapse for the non-helical flow at  $\mathcal{K}r = 0$  but do not collapse for the highly helical flow at  $\mathcal{K}r = 0.9$ . The separation of the PDFs at  $\mathcal{K}r = 0.9$  is consistent with the statistics presented in eq. (10). All the characteristics of the energy distribution of the DNS are in good agreement with the properties predicted by the absolute equilibrium theory.

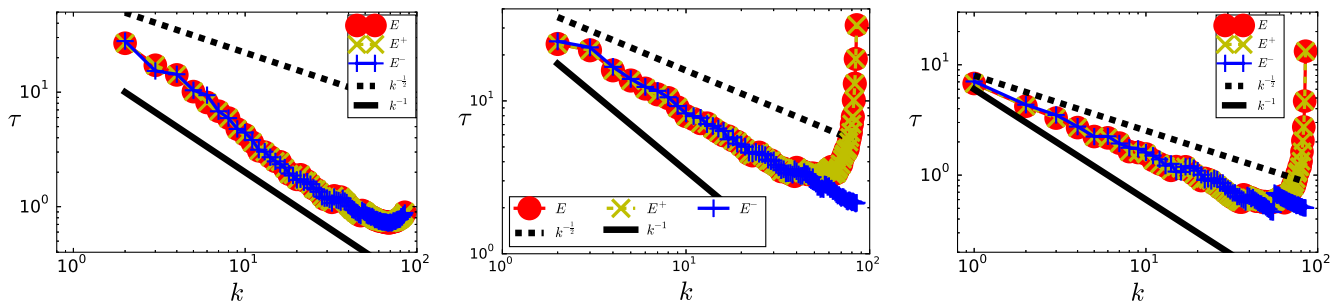


Figure 8: Correlation time of DNS of general-periodic solutions of the truncated Euler equation. Left) Non-helical flow  $\mathcal{K}r = 0$ . Center) Slightly helical flow  $\mathcal{K}r = 0.85$ . Right) Highly helical flow  $\mathcal{K}r = 0.9$ .

The last property that will be examined concerns the evolution of the correlation time as the flow becomes highly helical ( $\mathcal{K}r \rightarrow 1$ ). The thermalization theory, presented in sec. II, predicts that, as the system becomes highly helical, the energy-based correlation time ( $\tau_k^E$  in eq. (13)) should transition to a helicity-based correlation time ( $\tau_k^H$  in eq. (14)) in intermediate scales  $(1 - \mathcal{K}r) \ll k/k_M \ll 1$ . With the current computational power, it is difficult to show the same number of orders of magnitude as in fig. 1. Consequently, the results presented in fig. 8 are not able to show both scaling laws for a given  $\mathcal{K}r$ . The left panel of fig. 8 presents the correlation time of a non-helical flow at  $\mathcal{K}r = 0$  while the right panel of fig. 8 presents the correlation time of a highly helical flow at  $\mathcal{K}r = 0.9$ . The correlation time of the non-helical flow exhibits a  $k^{-1}$ -scaling law characteristic of an energy-based correlation time, while the correlation time of the highly helical flow is closer to a  $k^{-\frac{1}{2}}$ -scaling law characteristic of a helicity-based. Additionally, in the right panel of fig. 8, the correlation time peaks in the small scales, which is characteristic of the localization of the energy near  $k_M$  of helical flows. In the highly helical case, the difference between the positive and negative helical components of the velocity can also be observed in the small scales. While both helical components collapse in the non-helical case, they are different in the small scales in the highly helical case. All these observations are in agreement with the correlation time predicted by the thermalization theory. DNS were also performed at higher Kraichnan numbers and showed a persistence of the helicity-based correlation time.

Even though the transition of the scaling law is hard to observe in the DNS carried out, results indicate that the transition of correlation time regime occurs for Kraichnan numbers in the range  $0.8 \leq \mathcal{K}r \leq 0.9$ . The center panel of fig. 8 shows that for slightly less helical flows with  $\mathcal{K}r = 0.85$ , the correlation follows a power law with an exponent between  $-1$  and  $-\frac{1}{2}$ . A clear visualization of the transition is demanding in computational power, since it occurs on nearly one order of magnitude in the left panel of fig. 1.

#### IV. NAVIER-STOKES DNS

Because DNS of the *NSE* must have a converged spectrum at wavenumbers larger than the forcing wavenumber, their properties cannot be assessed with scale separations as large as those of DNS of the *TEE*. Using the same codes as in the previous section, we now turn to the study of how the PDF, the standard deviation and the correlation time behave in the large scales for DNS of the *NSE*. We will also compare these results with the observation made on DNS of the *TEE*.

### A. No helicity: Taylor-Green flows

*TG* flows are studied with different forcing wavenumbers  $k_f \in \{11\sqrt{3}; 35\sqrt{3}; 59\sqrt{3}\}$ . The forcing was imposed on the flow by fixing to 0.125 the amplitude of the odd modes  $[k_f, k_f, k_f]/\sqrt{3}$ . The other parameter of the system is the viscosity  $\nu$  which was also adjusted to reach a turbulent regime. To compare the properties of flows at different forcing wavenumbers, the Reynolds number  $Re = U/(\nu k_f)$  was set to 6.56.

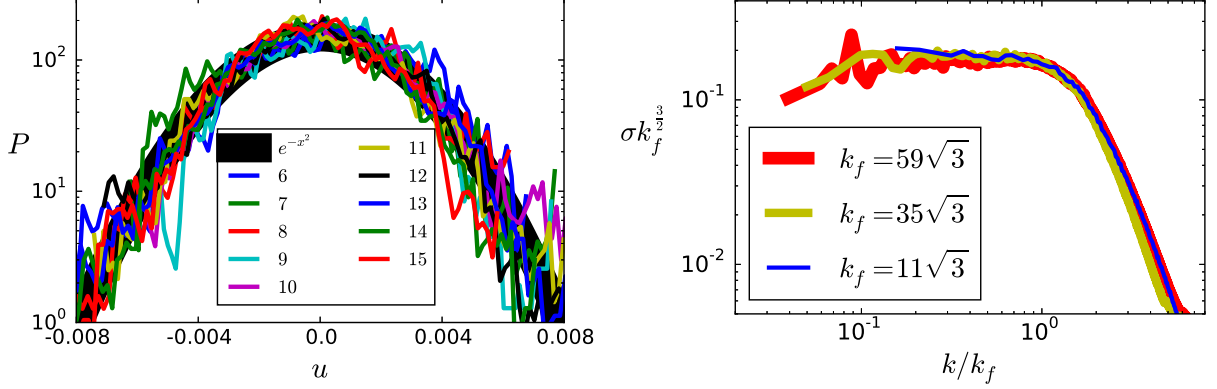


Figure 9: PDF of modes of Taylor-Green symmetric DNS of the forced Navier-Stokes equation with a forcing wavenumber at  $k_f = 11\sqrt{3}$ . Left) PDF of even modes with one degree of freedom at scales larger than the forcing scale. Right) Standard deviation of the velocity modes.

Fig. 9 represents some properties of the PDF of velocity modes with one degree of freedom in the six planes  $k_x \in \{0; 1\}$ ,  $k_y \in \{0; 1\}$  or  $k_z \in \{0; 1\}$ . These PDFs have a clear Gaussian behavior as highlighted by their parabolic shape on the semi-logarithmic plot in the left panel of fig. 9. The datasets in the left panel, representing modes with  $k < k_f$ , collapse on the same curve, which indicates that their standard deviation is identical. These two trends are also observed in the right panel of fig. 9, where the standard deviation of the PDFs are represented for different forcing scales. In the right panel of fig. 9, the standard deviations,  $\sigma$ , are compensated by a factor  $k_f^{3/2}$  to take into account that the total energy is spread out on more modes as the forcing wavenumber increases. The wavenumber is also rescaled by the forcing wavenumber in order to compare the results. Using this scaling, the datasets at different resolutions collapse on the same curve. At large scales, the compensated standard deviation plateaus, indicating an analogue of the equipartition in energy of absolute equilibrium without helicity  $\mathcal{K}r = 0$ . Below the forcing scale, the standard deviation rapidly decreases because of the forward cascade and viscosity.

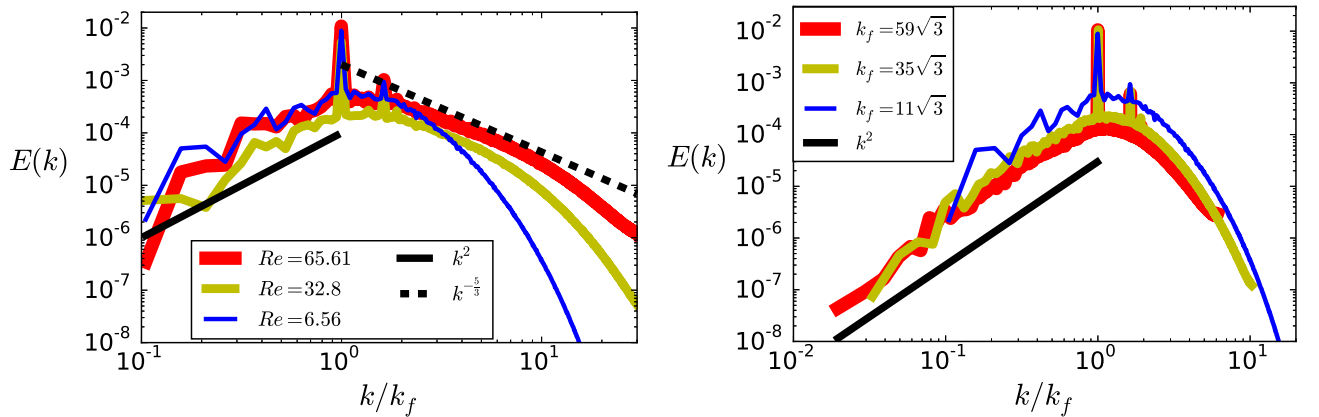


Figure 10: Energy spectrum of Taylor-Green symmetric flows solutions of the forced Navier-Stokes equation. Left) Fixed forcing mode  $k_f = 11\sqrt{3}$  at different Reynolds numbers  $Re \in \{11\sqrt{3}; 35\sqrt{3}; 59\sqrt{3}\}$ . Right) Fixed Reynolds number  $Re = 6.56$  at different forcing modes  $k_f \in \{11\sqrt{3}; 35\sqrt{3}; 59\sqrt{3}\}$ .

Energy equipartition in the large scale modes can directly be observed in the right panel of fig. 9. It can also indirectly be observed in the energy spectrum presented in fig. 10. Since energy shells contain a number of modes proportional

to their surface,  $4\pi k^2$ , systems satisfying equipartition in energy should have an energy spectrum proportional to  $k^2$ . The spectra presented on both panels of fig. 10 are thus consistent with equipartition in energy. In left panel of fig. 10, the energy spectrum is presented at different Reynolds numbers for a fixed forcing wavenumber  $k_f = 11\sqrt{3}$ . At the largest Reynolds number, the energy spectrum reaches the Kolmogorov's  $k^{-5/3}$ -scaling in the inertial range and has also the equipartition  $k^2$ -scaling in the thermalization domain. Even though Kolmogorov's scaling is not present in the other curves with smaller Reynolds numbers, the equipartition scaling law is still observable in the large scales. The smallest Reynolds number was then used to compute the DNS of the right panel of fig.10 where the wavenumber varies at fixed Reynolds number. The equipartition scaling of the energy spectrum can be observed on the three forcing wavenumbers used. The curve with the largest forcing scale,  $k_f = 59\sqrt{3}$ , shows that the energy spectrum follows a  $k^2$ -scaling for nearly two decades.

We now turn to the temporal correlation of the flows presented in fig. 11. The left panel shows the dependence on viscosity of the correlation time for flows forced at  $k_f = 11\sqrt{3}$ . The correlations are computed using the algorithm presented in subsec. III A 1. In the small scales, the correlation time slowly decreases as viscosity decreases whereas the correlation time rapidly stabilizes on a  $k^{-1}$ -power law in the large scales. The major peak observed in the flow does not correspond to the forcing wavevector which is not located on the planes used to compute the correlation time. This peak corresponds to a harmonic of the forcing located in one of the planes used in the correlation time procedure. At high Reynolds number, in the large scales, the correlation time aligns on a curve, which is consistent with the energy-based correlation time  $k^{-1}$ -scaling.

The  $k^{-1}$ -scaling law of the correlation time can be observed on the right panel of fig. 11 which shows the correlation time for three scale separations  $k_f = \{11\sqrt{3}; 35\sqrt{3}; 59\sqrt{3}\}$ . The Reynolds number used in these DNS is based on the smallest viscosity used in the left panel of fig. 11. The correlation times for the three scale separations collapse on the  $k^{-1}$ -power law. The data at the largest forcing wavenumber  $k_f = 59\sqrt{3}$  shows a trend which strongly agrees with the energy-based correlation time  $k^{-1}$ -scaling.

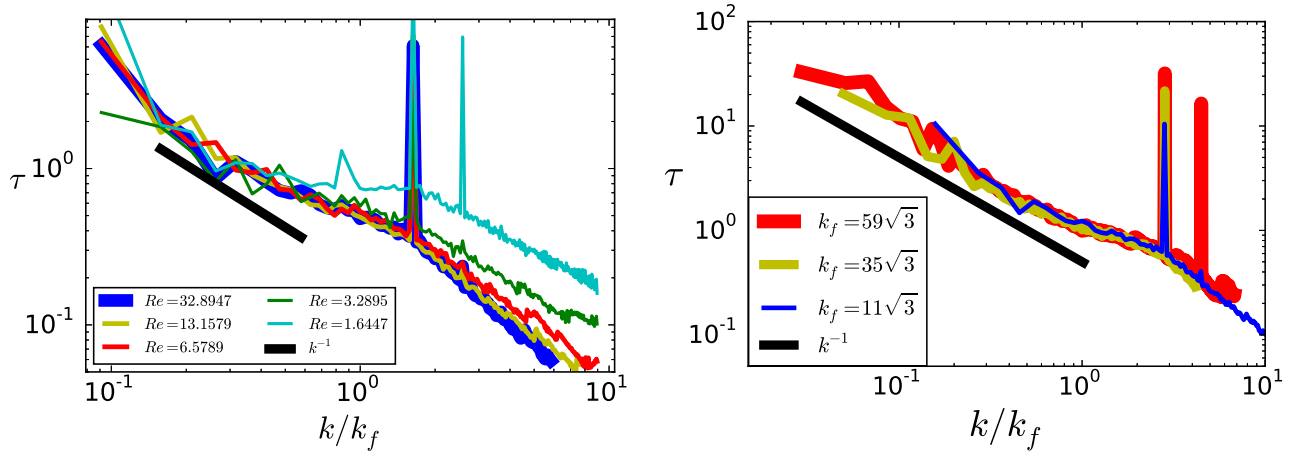


Figure 11: Correlation time of Taylor-Green symmetric DNS of the forced Navier-Stokes equation. Left) Different Reynolds numbers at fixed forcing wavenumber  $k_f = 11\sqrt{3}$ . Right) Different forcing wavenumber  $k_f \in \{11\sqrt{3}; 35\sqrt{3}; 59\sqrt{3}\}$  at fixed Reynolds number.

## B. Helical flows: $ABC$ flows

In order to study the impact of helicity on the velocity modes in large scales, DNS were carried out on general-periodic flows solutions of the  $NSE$  given at eq. (2) with an  $ABC$  forcing [27]

$$F_x^{ABC} = F_0(C \sin k_f z + B \cos k_f y), \quad F_y^{ABC} = F_0(A \sin k_f x + C \cos k_f z), \quad F_z^{ABC} = F_0(B \sin k_f y + A \cos k_f x). \quad (22)$$

where  $F_0$  is the intensity of the forcing. The three dimensionless parameters  $A$ ,  $B$  and  $C$  were set to one. The main characteristic of  $ABC$  flows is their Beltrami property:  $\nabla \times F^{ABC} = k_f F^{ABC}$ . This property makes them exact (but in general unstable) solutions of the  $TEE$ . All the  $ABC$  DNS presented are done at  $k_f = 20$ . A non-helical variant of the  $ABC$  forcing, that we will be referred to as the  $CBA$  forcing, can be built by switching the sine components of the  $ABC$  forcing to cosine components.

$$F_x^{CBA} = F_0(C \cos k_f z + B \cos k_f y), \quad F_y^{CBA} = F_0(A \cos k_f x + C \cos k_f z), \quad F_z^{CBA} = F_0(B \cos k_f y + A \cos k_f x). \quad (23)$$

The *CBA* forcing has already been used as a non-helical reference of the *ABC* flow in [28]. At fixed coefficients, the *CBA* forcing has the same energy as the *ABC* forcing.

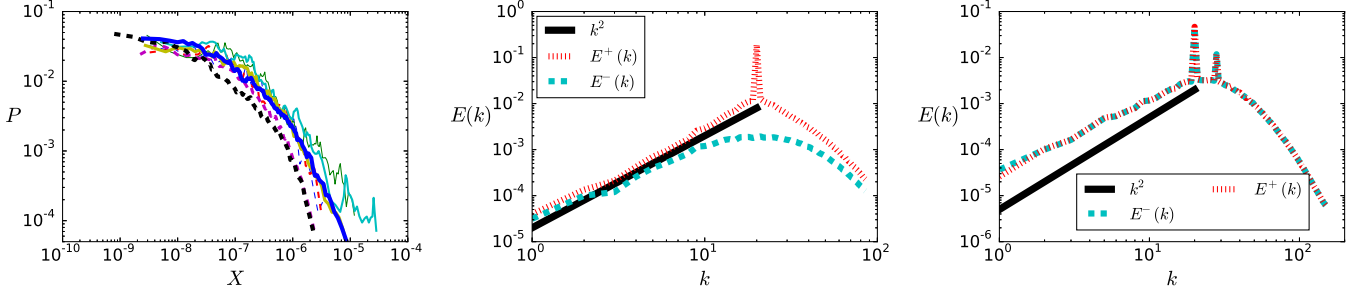


Figure 12: Statistical characteristics of general-periodic DNS of the Navier-Stokes equation. Left) *ABC* forcing, PDF of modes before the forcing scale. The full lines represent the positive helical components of the velocity and the dashed lines represent the negative helical components of the velocity. Center) *ABC* forcing, energy spectrum of positive and negative helical components of the velocity. Right) *CBA* forcing, energy spectrum of positive and negative helical components of the velocity.

The PDFs of the positive and negative helical components of the modes in the large scales are presented in the left panel of fig. 12 for DNS of the *NSE* with an *ABC* forcing. The positive helical component of the velocity is represented with full lines and the negative helical component of velocity is represented with dashed lines. All PDFs plateau near zero and have an fast decay at high values. Because general-periodic DNS do not reach the same scale separation and Reynolds number as *TG* symmetric DNS, the comparison with the  $\chi^2_2$ -distribution is not as clear as in fig. 9. The PDFs of the two helical components do not have the same exponential tail as observed in absolute equilibrium solutions of the *TEE*. Since solutions of the *NSE* are not as helical as the solution of the *TEE* considered in the previous section, the separation of the tail of the distributions is not as wide as in the case of absolute equilibrium solutions of the *TEE*. The center panel of fig. 12 represents the energy spectrum of the two helical components of DNS of the *NSE* with an *ABC* forcing. The positive helical component of the velocity has more energy than its negative counterpart, which is consistent with the separation of the tail of the distribution presented in the left panel. Both components follow a  $k^2$ -scaling consistent with equipartition. In the large scales, the general features of the modes match the properties of absolute equilibrium solutions of the *TEE*. The right panel of fig. 12 represents the energy spectrum of the two helical components of DNS of the *NSE* with a *CBA* forcing. The energy spectrum is not as close to the  $k^2$ -scaling as the energy spectrum resulting from an *ABC* forcing. We note that the energy spectrum of the non-helical *TG* symmetric flows, presented in the right panel of fig. 10, deviates from the  $k^2$ -scaling at the smallest scale separations. The convergence study carried out in the right panel of fig. 4 indicates that such a deviation can happen at small scale separations.

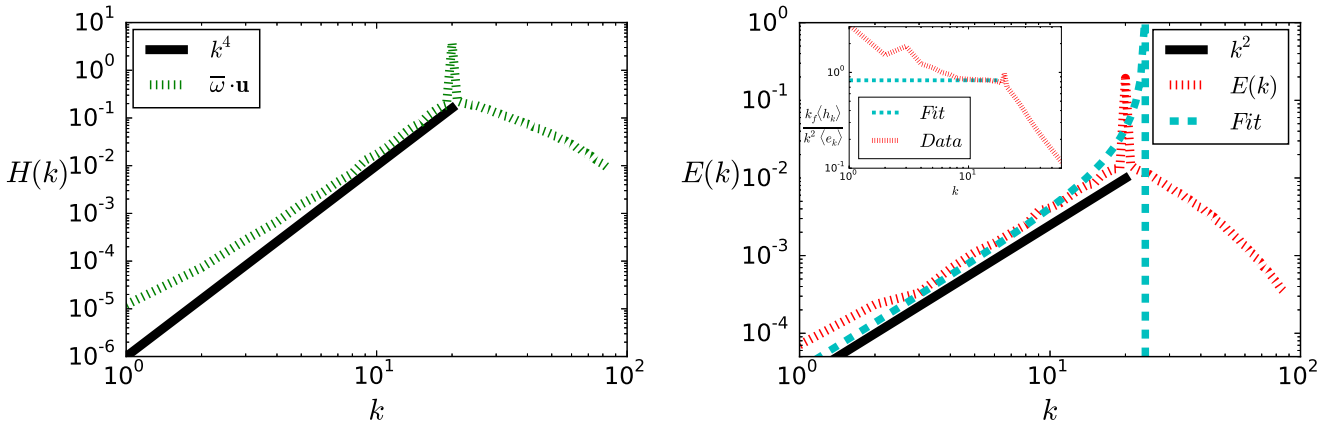


Figure 13: Spectrum of general-periodic DNS of the Navier-Stokes equation with an *ABC* forcing. Left) Helicity spectrum in dotted line and the absolute equilibrium power law in full line. Right) Energy spectrum in dotted line with absolute equilibrium power law in full line and absolute equilibrium fit in dashed line. The insert represents  $k_f \langle h_{\mathbf{k}} \rangle / (k^2 \langle e_{\mathbf{k}} \rangle)$  and the asymptotic value used to make the absolute equilibrium fit.

The left panel of fig. 13 represents the helicity spectrum of a solution of the Navier-Stokes equation with an *ABC*

forcing. In the scales slightly larger than the forcing scale, the helicity spectrum is in good agreement with the  $k^4$ -power law of the absolute equilibrium prediction. But in the largest scale, the helicity spectrum has a deviation from the  $k^4$ -power law.

To compare absolute equilibrium solutions of the *TEE* and the large scale modes of solutions of the *NSE*, we introduce an analogue of the Kraichnan number for the *NSE*. The equivalent of the maximal wavenumber  $k_M$  in the truncated Euler problem is assumed to be the forcing wavenumber  $k_f$  in the case of the *NSE*. Two expressions can be used to compute the local Kraichnan number: either  $k_f \langle h_{\mathbf{k}} \rangle / (k^2 \langle e_{\mathbf{k}} \rangle)$  coming from eq. (9) or  $k_f (\langle e_{\mathbf{k}}^+ \rangle - \langle e_{\mathbf{k}}^- \rangle) / (k (\langle e_{\mathbf{k}}^+ \rangle + \langle e_{\mathbf{k}}^- \rangle))$  coming from eq. (10). Both expressions are equivalent and give the same numeric results presented in the insert of the right panel of fig. 13. The local Kraichnan number is not independent of the wavenumber and has an important peak in the large scales. As the wavenumber reaches the forcing wavenumber, the local local Kraichnan number goes to a constant value equal to 0.83. The result is consistent with the  $|\mathcal{K}r| \leq 1$  bound of absolute equilibrium solutions. This asymptotic value is then used to plot the absolute equilibrium fit in the right panel of fig. 13. In the large scales, the data from the DNS is slightly above the fit, while the data is below the fit near the forcing wavenumber. The difference between the fit and the data near the forcing wavenumber can be related to the presence of the forcing. The difference found in the large scales could be related to finite size effects such as three-mode interaction with the forcing like in [12].

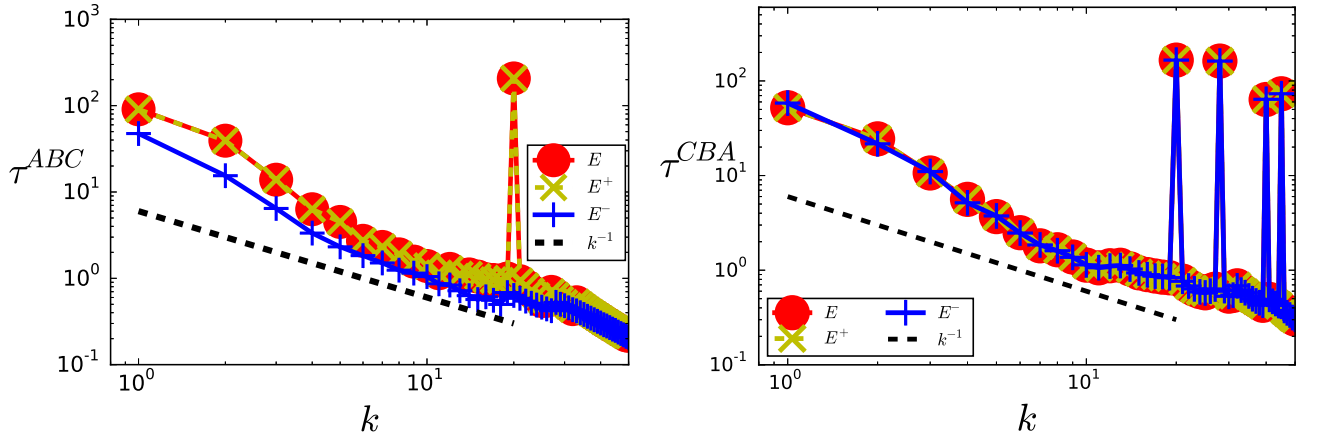


Figure 14: Correlation time of general-periodic DNS of the Navier-Stokes equation. Left) *ABC* forcing. Right) *CBA* forcing.

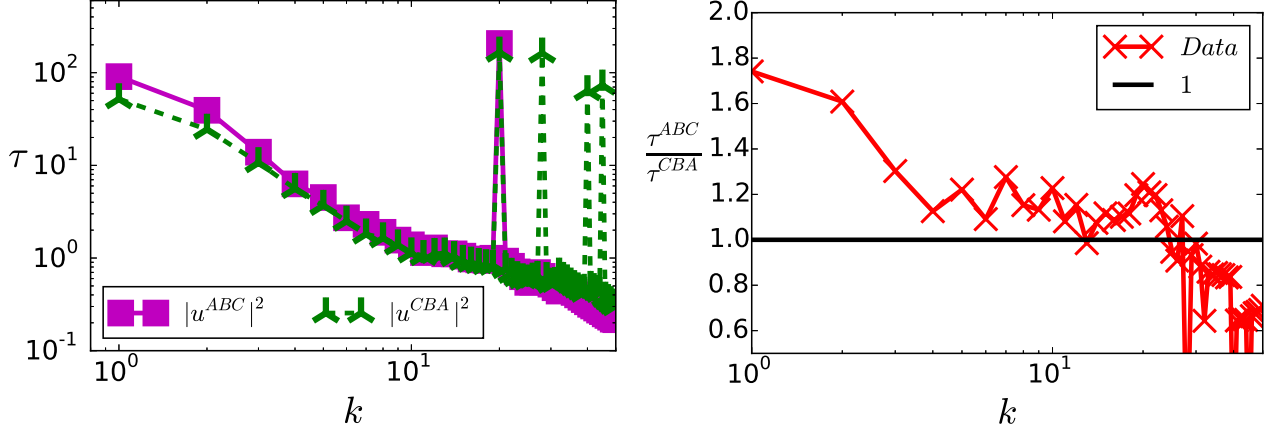


Figure 15: Comparison of the correlation time of  $[0; 2\pi]^3$ -periodic DNS solutions of the Navier-Stokes equation forced with *ABC* and *CBA* forcings. Left) Energy spectrum. Right) Energy ratio.

The correlation time of DNS of the *NSE* with an *ABC* forcing increases in the large scales as shown in the left panel of fig. 14. In the inertial domain, the correlation time decreases as the wavenumber increases. These observations are consistent with the results of helical DNS of the *TEE* and the *TG* symmetric DNS of the the *NSE*. However, the correlation time has some elements which do not appear in the helical DNS of the *TEE* presented in fig. 8.

The correlation time of positive helical components of the velocity is always greater than its negative counterpart, especially in the large scales. This separation between the correlation time of the different helical components is not observed in the right panel of fig. 14 representing DNS of the *NSE* with a *CBA*. Contrary to the *ABC* forced flow, the correlation times of *CBA* forced flows exhibit a set of peaks in the inertial domain corresponding to harmonics of the forcing. For the *ABC* forcing and *CBA* forcing, the correlation time in the large scales deviates from the  $k^{-1}$ -power law observed in DNS of *TEE*. However, for similar scale separations, the results from *TG* DNS also deviated from the  $k^{-1}$ -power law in the left panel of fig. 11. Fig. 15 compares the correlation times of the *ABC* forcing and *CBA* forcing. The correlation time of the two flows seems very close when observing the energy spectrum presented in the left panel. However, the ratio presented in the right panel shows that the correlation times of the helical *ABC* forcing are larger than their non-helical *CBA* counterparts. The differences between the two correlation times reaches nearly twenty percents for all the wavenumbers smaller than the forcing wavenumber and is much more important in the two shells with smallest  $k$ .

## V. CONCLUSION

In this study, we examined analytically and numerically the temporal dynamics of absolute equilibrium solutions of the truncated Euler equation and compared them to the large scale modes of solutions of the Navier-Stokes equation. We calculated the Eulerian parabolic auto-correlation time of velocity modes of absolute equilibrium solutions of the *TEE* under the assumption that the velocity modes follow a Boltzmann-Gibbs distribution. For non-helical or slightly helical flow,  $|\mathcal{K}r| < 0.8$ , the correlation time decreases inversely proportionally to the wavenumber and the square root of energy  $\tau \propto 1/(kE^{1/2})$ . On the other hand, when the flow is highly helical  $|\mathcal{K}r| > 0.9$ , the correlation time depends on the helicity and is inversely proportional to the square root of the wave number  $\tau \propto 1/(k^{1/2}H^{1/2})$ . This new power law behavior holds for wavenumbers that satisfy  $(1 - \mathcal{K}r) \ln(1 - \mathcal{K}r) \ll k/k_M \ll 1$ , while the  $k^{-1}$  is recovered at even smaller wavenumbers. These results and the assumptions on which they were based were tested against the results of DNS of the *TEE* showing excellent agreement: the PDFs of the modes of velocity displayed the characteristics of Gaussian variables, their energy spectrum followed the laws predicted by the absolute equilibrium theory, and the two predicted power laws for the correlation time for helical and non-helical flows were recovered. We have thus demonstrated that, in the long time limit, the *TEE* thermalizes to an absolute equilibrium state whose statistics and time-correlation can be derived from a Boltzmann-Gibbs distribution.

The results are less clear for the large scales of the forced *NSE*. Simulations using the non-helical *TG* geometry, that allowed us to reach larger scale separation, displayed considerable agreement with the absolute equilibrium. The velocity modes at large scales followed Gaussian distributions with standard deviations consistent with equipartition; the correlation time followed a power law compatible with the  $k^{-1}$  scaling for almost two decades. This is in agreement with the absolute equilibrium at large scales. The agreement however was less strong with the results of DNS of general-periodic flows. The large scale spectra were compatible with the absolute equilibrium predictions for a limited range. The largest scales deviated significantly, being more energetic and more helical than predicted. Note that this deviation was also observed in [10]. Furthermore, while the correlation time of the helical flows was shown to decrease with helicity as in thermalization theory the measured correlation time deviates significantly from the predicted  $k^{-1}$  and  $k^{-1/2}$  power laws. We note however that a similar deviation is also observed in non-helical *TG* symmetric DNS at the smallest boxes used (see fig. 10), so these deviations could be due to insufficient scale separation.

The reason for which the largest scales of Navier-Stokes solutions deviate from absolute equilibrium still remains an open question. As discussed above, a possible cause for this deviation could be related to the range in the large scales or the range of Reynolds number. For the moment, however, we can not exclude the possibility that large scales lack universality with respect to forcing or that large scales instabilities spoil the absolute equilibrium properties. These questions are left for future studies.

## ACKNOWLEDGMENTS

This work was granted access to the HPC resources of MesoPSL financed by the Region Ile de France and the project Equip@Meso (reference ANR-10-EQPX-29-01) of the programme Investissements d'Avenir supervised by the Agence Nationale pour la Recherche and the HPC resources of GENCI-TGCC-CURIE & GENCI-CINES-JADE (Project No. x20162a7620) where the present numerical simulations have been performed. The authors are grateful to Pablo MININNI and Patricio CLARK DI LEONI for their useful discussion on spatio-temporal spectra.

## VI. APPENDIX: CORRELATION TIME – PARABOLIC HYPOTHESIS

The derivation of the correlation time can be done using a projection operator on incompressible flows, as in ref. [8]. However, this method is not able to assess the properties of the helical components of the velocity. In order to quantify these properties, the standard framework is the Craya-Herring helical basis [15, 16]. Within this decomposition, the  $TEE$  is expressed as

$$(\partial_t u_{\mathbf{k}}^{s_{\mathbf{k}}})^* = \sum_{\substack{\mathbf{k}+\mathbf{p}+\mathbf{q}=0 \\ s_{\mathbf{p}}, s_{\mathbf{q}}}} (s_{\mathbf{p}}p - s_{\mathbf{q}}q) \left( -\frac{1}{4} \mathbf{h}_{\mathbf{k}}^{s_{\mathbf{k}}} \cdot \mathbf{h}_{\mathbf{p}}^{s_{\mathbf{p}}} \times \mathbf{h}_{\mathbf{q}}^{s_{\mathbf{q}}} \right) u_{\mathbf{p}}^{s_{\mathbf{p}}} u_{\mathbf{q}}^{s_{\mathbf{q}}} = \sum_{\substack{\mathbf{k}+\mathbf{p}+\mathbf{q}=0 \\ s_{\mathbf{p}}, s_{\mathbf{q}}}} C_{\mathbf{k}\mathbf{p}\mathbf{q}}^{s_{\mathbf{k}}s_{\mathbf{p}}s_{\mathbf{q}}} u_{\mathbf{p}}^{s_{\mathbf{p}}} u_{\mathbf{q}}^{s_{\mathbf{q}}}, \quad (24)$$

where  $s_{\mathbf{k}}$  denotes the sign of the helical component at mode  $\mathbf{k}$ ,  $u_{\mathbf{k}}^{s_{\mathbf{k}}}$  denotes the helical component of the velocity of sign  $s_{\mathbf{k}}$  at mode  $\mathbf{k}$  and  $\mathbf{h}_{\mathbf{k}}^{s_{\mathbf{k}}}$  denotes the complex unitary helical vector of the Craya-Herring basis satisfying:  $\nabla \times \mathbf{h}_{\mathbf{k}}^{s_{\mathbf{k}}} = s_{\mathbf{k}} k \mathbf{h}_{\mathbf{k}}^{s_{\mathbf{k}}}$ . The Craya-Herring tensor  $C_{\mathbf{k}\mathbf{p}\mathbf{q}}^{s_{\mathbf{k}}s_{\mathbf{p}}s_{\mathbf{q}}}$  is symmetric on its last two variables:  $C_{\mathbf{k}\mathbf{p}\mathbf{q}}^{s_{\mathbf{k}}s_{\mathbf{p}}s_{\mathbf{q}}} = C_{\mathbf{k}\mathbf{q}\mathbf{p}}^{s_{\mathbf{k}}s_{\mathbf{q}}s_{\mathbf{p}}}$ , and also satisfies:  $C_{\mathbf{k}\mathbf{p}\mathbf{p}}^{s_{\mathbf{k}}s_{\mathbf{p}}s_{\mathbf{p}}} = 0$ . With the Craya-Herring helical decomposition, the average correlation of the temporal derivative of the velocity can be derived with the assumption that all helical components are independent Gaussian variables. The derivation leads to

$$\langle |\partial_t \bar{u}_{\mathbf{k}}^{s_{\mathbf{k}}}|^2 \rangle = \left\langle \sum_{\substack{\mathbf{k}+\mathbf{p}_1+\mathbf{q}_1=0 \\ s_{\mathbf{p}_1}, s_{\mathbf{q}_1}}} \sum_{\substack{\mathbf{k}+\mathbf{p}_2+\mathbf{q}_2=0 \\ s_{\mathbf{p}_2}, s_{\mathbf{q}_2}}} C_{\mathbf{k}\mathbf{p}_1\mathbf{q}_1}^{s_{\mathbf{k}}s_{\mathbf{p}_1}s_{\mathbf{q}_1}} u_{\mathbf{p}_1}^{s_{\mathbf{p}_1}} u_{\mathbf{q}_1}^{s_{\mathbf{q}_1}} \left[ C_{\mathbf{k}\mathbf{p}_2\mathbf{q}_2}^{s_{\mathbf{k}}s_{\mathbf{p}_2}s_{\mathbf{q}_2}} u_{\mathbf{p}_2}^{s_{\mathbf{p}_2}} u_{\mathbf{q}_2}^{s_{\mathbf{q}_2}} \right]^* \right\rangle \quad (25)$$

$$= \sum_{s_1, s_2} \mathcal{S}^{s_1 s_2} \quad \text{where} \quad \mathcal{S}^{s_1 s_2} = \sum_{\substack{\mathbf{k}+\mathbf{p}+\mathbf{q}=0 \\ s_{\mathbf{p}}=s_1, s_{\mathbf{q}}=s_2}} 2 \left| C_{\mathbf{k}\mathbf{p}\mathbf{q}}^{s_{\mathbf{k}}s_{\mathbf{p}}s_{\mathbf{q}}} \right|^2 \langle |u_{\mathbf{p}}^{s_{\mathbf{p}}}|^2 \rangle \langle |u_{\mathbf{q}}^{s_{\mathbf{q}}}|^2 \rangle. \quad (26)$$

where  $\mathcal{S}^{s_1 s_2}$  corresponds to the sum of the triadic interact of sign  $s_1$  and  $s_2$ .

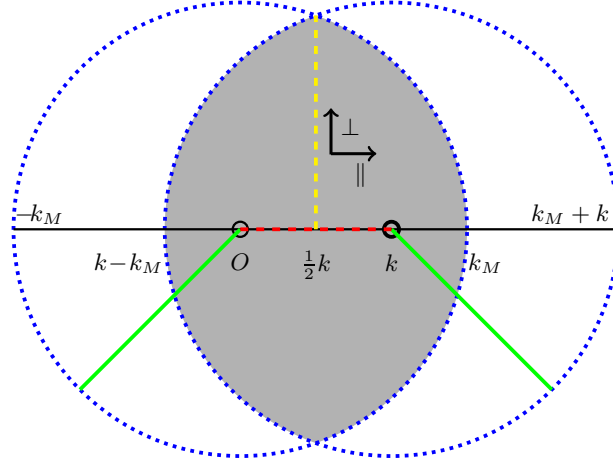


Figure 16: Diagram of a cut of the integration domain. The dark surface corresponds to the integration domain. The dotted lines correspond to the limit of the circles of radius  $k_M$  and of center 0 or  $k$ . The thick full line corresponds to radii of the previously described circles. The dark dashed line corresponds to the distance between the center of the two circles. The bright dashed line corresponds to the maximal length possible for  $q_{\perp}$ .

In eq. (26), the truncation condition,  $\mathbf{u}(k > k_M) = 0$ , has not been applied to the velocity fields. The velocity appears in the equation within the expression of the average energy with two indices  $\mathbf{p}$  and  $\mathbf{q}$ , therefore the summation must be done at  $p \leq k_M$  and  $q \leq k_M$ . The domain prescribed by these conditions corresponds to the intersection of two spheres of radii  $k_M$  and centers  $\mathbf{p}$  and  $\mathbf{q}$ . The triadic condition,  $\mathbf{k} + \mathbf{p} + \mathbf{q} = 0$ , also implies that the summation over  $\mathbf{p}$  and  $\mathbf{q}$  can be done over  $\mathbf{q}$  at fixed  $\mathbf{p} = \mathbf{k} - \mathbf{q}$ . The domain of summation is represented in fig. 16. This domain is invariant by rotation along the axis defined by  $\mathbf{k}$  in fig. 16. The centers of the two spheres are also located on this direction. The coefficients of the sum in eq. (26) are unaffected by the rotation. The summation can thus be performed with the variables  $q_{\perp}$  and  $q_{\parallel}$  where  $q_{\perp}$  is the projection of the wavevector along the plane orthogonal to  $\mathbf{k}$  and  $q_{\parallel}$  is the projection of the wavevector along the axis of rotation. Taking this new coordinate system, the

derivation can be simplified by converting the discrete sum into an integral using the equivalence

$$\sum_{\mathbf{k}+\mathbf{p}+\mathbf{q}=0} \iff \int_{-(1-\frac{1}{2}m)}^{1-\frac{1}{2}m} dq_{\parallel} \int_0^{1-(|q_{\parallel}|+\frac{1}{2}m)^2} \pi dq_{\perp}^2 \quad \text{where } m = \frac{k}{k_M}. \quad (27)$$

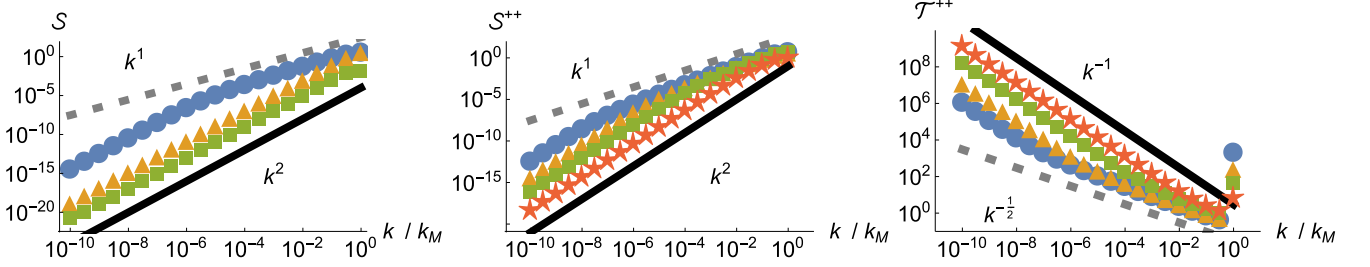


Figure 17: Triadic interaction as a function of the wavenumber and associated correlation time. Left) At  $\mathcal{K}r = 1 - 10^{-6}$ ,  $\mathcal{S}^{-+}$  plotted with squares,  $\mathcal{S}^{+-}$  plotted with triangle,  $\mathcal{S}^{++}$  plotted with discs,  $k^1$  plotted with a dashed line,  $k^2$  plotted with a full line. Center)  $\mathcal{S}^{++}$  plotted at  $\mathcal{K}r = 1 - 10^{-8}$  with discs, at  $\mathcal{K}r = 1 - 10^{-6}$  with triangles, at  $\mathcal{K}r = 1 - 10^{-2}$  with squares, at  $\mathcal{K}r = 1 - 10^{-2}$  with stars,  $k^1$  with a dashed line,  $k^2$  with a full line. Right)  $\mathcal{T}^{++}$  plotted at  $\mathcal{K}r = 1 - 10^{-8}$  with discs, at  $\mathcal{K}r = 1 - 10^{-6}$  with triangles, at  $\mathcal{K}r = 1 - 10^{-2}$  with squares, at  $\mathcal{K}r = 1 - 10^{-2}$  with stars,  $k^{-\frac{1}{2}}$  with a dashed line,  $k^{-1}$  with a full line.

This integral can be computed exactly when  $\mathcal{K}r = 0$  for  $m \ll 1$ , the parabolic correlation time is then expressed as

$$\tau_{\mathbf{k}}^{s_{\mathbf{k}}} = \sqrt{\frac{\langle |u_{\mathbf{q}}^{s_{\mathbf{q}}}|^2 \rangle}{\langle |\partial_t \tilde{u}_{\mathbf{k}}^{s_{\mathbf{k}}}|^2 \rangle}} = \sqrt{\frac{45\alpha}{112} \frac{1}{k}} = \sqrt{\frac{15\pi C_N}{14} \frac{1}{k\sqrt{E_{tot}}}}. \quad (28)$$

Since  $E_{tot} \propto \alpha^{-1}$ , the correlation time follows the energy-based scaling-law.

When  $\mathcal{K}r \neq 0$ , the final integral can be computed using Mathematica for the different helical triadic interactions as shown in fig. 17 for highly helical flows. Instead of computing all the terms corresponding to all different possible triads in the sum, the graph shows the computation triad with different helical signs. The left plot of fig. 17 shows three possible sums:  $\mathcal{S}^{++}$  plotted with discs,  $\mathcal{S}^{+-}$  plotted with triangles and  $\mathcal{S}^{-+}$  plotted with squares. The  $\mathcal{S}^{-+}$  sum has exactly the same values as the  $\mathcal{S}^{+-}$  sum for symmetry reasons. The  $\mathcal{S}^{++}$  sum dominates the other terms and has a  $k^1$ -scaling at large wavenumbers consistent with a helicity-based correlation time, and a  $k^2$ -scaling at small wavenumbers consistent with an energy-based correlation time. All other terms follow a  $k^2$ -scaling. The center plot of fig. 17 shows the evolution of the  $\mathcal{S}^{++}$  for different Kraichnan numbers. As the Kraichnan number goes to one, the domain where the sum follows a  $k^2$ -scaling widens. The right plot of fig. 17 shows the evolution of the correlation time,  $\mathcal{T}^{++}$ , built using the sum  $\mathcal{S}^{++}$ . Its evolution is consistent with the evolution of the correlation time of the full velocity field presented in the left panel of fig. 1.

When the Kraichnan number goes to one, the *plus-plus* triadic interaction dominates the non-linear interaction in the *TEE*. Whether  $m \ll \epsilon \ll 1$  or  $\epsilon \ll m \ll 1$ , the correlation time follows the asymptotic expression

$$\mathcal{S}^{++} = 2\pi k^2 \alpha^{-2} \frac{-2 \ln \epsilon}{m - A\epsilon \ln \epsilon} \quad \text{with } A = \frac{15}{8} \quad \text{thus } \mathcal{T}^{++}(\mathbf{k}, s_{\mathbf{k}}) = \sqrt{\frac{\langle |u_{\mathbf{k}}^{s_{\mathbf{k}}}|^2 \rangle}{\mathcal{S}^{++}}} = \sqrt{\frac{A(1 - \mathcal{K}r) - \frac{k}{k_M \ln(1 - \mathcal{K}r)}}{4\pi\alpha^{-1}k^2(1 - s_{\mathbf{k}}\mathcal{K}r\frac{k}{k_M})}}. \quad (29)$$

In the domain where  $(1 - \mathcal{K}r) \ll \frac{k}{k_M} \ll 1$ , the correlation time follows a helicity-based scaling-law.

## VII. APPENDIX: TAYLOR-GREEN SYMMETRIES

In addition to the condition listed below eq. (19), *TG* symmetries [21] impose that

$$u^y(k_x, k_y, k_z) = (-1)^{p+1} u_x(k_y, k_x, k_z) \quad \text{and} \quad u_z(k_x, k_y, k_z) = (-1)^{p+1} u_z(k_y, k_x, k_z), \quad (30)$$

where  $p$  characterizes the parity of the mode:  $p = 1$  if  $k_x, k_y, k_z$  are all even and  $p = 0$  if  $k_x, k_y, k_z$  are all odd.

Since the flows studied are also incompressible, they also satisfy  $\nabla \cdot \mathbf{u} = 0 \iff k_x u_x + k_y u_y + k_z u_z = 0$ .

In a few special cases, modes of *TG* symmetric flows depend on only one independent variable



- $k_x = k_y$  and  $r = 0$ :  $\mathbf{u}^{odd}(k_x, k_x, k_z) = (\mathbf{e}_x - \mathbf{e}_y)\psi_0(k_x, k_z)$  where  $\psi_0$  is a real field.
- $k_x = k_y$  and  $r = 1$ :  $\mathbf{u}^{even}(k_x, k_x, k_z) = (k_z(\mathbf{e}_x + \mathbf{e}_y) - (k_x + k_y)\mathbf{e}_z)\psi_1(k_x, k_x, k_z)$  where  $\psi_1$  is a real field.
- $k_x = 0$ :  $\mathbf{u}(0, k_y, k_z) = (k_z\mathbf{e}_y - k_y\mathbf{e}_z)\psi_2(k_y, k_z)$  where  $\psi_2$  is a real field.
- $k_y = 0$ :  $\mathbf{u}(k_x, 0, k_z) = (k_z\mathbf{e}_x - k_x\mathbf{e}_z)\psi_3(k_x, k_z)$  where  $\psi_3$  is a real field.
- $k_z = 0$ :  $\mathbf{u}(k_x, k_y, 0) = (k_y\mathbf{e}_x - k_x\mathbf{e}_y)\psi_4(k_x, k_y)$ , where  $\psi_4$  is a real field satisfying  $\psi_4(k_y, k_x) = -\psi_4(k_x, k_y)$ .

The vectors  $\mathbf{e}_\alpha$  with  $\alpha \in \{x; y; z\}$  denote the directions of the Cartesian basis.

In the other cases, the  $TG$  symmetric modes of flows only depend on two independent variables –  $\phi(k_x, k_y, k_z)$  and  $\phi(k_y, k_x, k_z)$ , where  $\phi$  is a real field – and can be written as

$$\mathbf{u}(k_x, k_y, k_z) = (k_z\mathbf{e}_x - k_x\mathbf{e}_z)\phi(k_x, k_y, k_z) + (-1)^{p+1}(k_z\mathbf{e}_y - k_y\mathbf{e}_z)\phi(k_y, k_x, k_z). \quad (31)$$

### VIII. APPENDIX: CHI-SQUARED DISTRIBUTION

A Gaussian distribution of average  $\mu$  and standard derivation  $\sigma$  has a probability density function defined by

$$G(X|\mu, \sigma) = \frac{1}{\sqrt{2\sigma^2\pi}} e^{-\frac{(X-\mu)^2}{2\sigma^2}}. \quad (32)$$

Chi-squared distributions are defined using  $g$  independent Gaussian variables. Let  $(G_i)_{i \in \llbracket 1; g \rrbracket}$  be independent, centered ( $\mu = 0$ ), reduced ( $\sigma = 1$ ) Gaussian variables. The sum of their squares,  $X = \sum_{i=1}^g G_i^2$ , is distributed according to the chi-squared distribution with  $g$  degrees of freedom denoted as  $\chi_g^2$  and defined by

$$\chi_g^2(X) = \frac{1}{2^{\frac{g}{2}} \Gamma_{Euler}(\frac{g}{2})} X^{\frac{g}{2}-1} e^{-\frac{X}{2}}. \quad (33)$$

where  $\Gamma_{Euler}$  denotes Euler's Gamma function. The power law of the probability density function at small  $X$  gives the number of degrees of freedom of the system, and the exponential fit at large  $X$  validates the Gaussian decay of the probability density function.

$$\log \chi_g^2(X) \underset{X \rightarrow 0}{=} \left(\frac{g}{2} - 1\right) \log(X) \quad \text{thus} \quad g \underset{X \rightarrow 0}{=} 2 \left(\frac{\log \chi_g^2(X)}{\log(X)} + 1\right) \quad (34)$$

### IX. APPENDIX: COMPUTATION OF THE CORRELATION TIME

In order to produce spatio-temporal spectrum, the velocity field is outputted at a regular time interval. These outputs form a dataset of the velocity field in the  $\mathbf{k} - t$  space. However, keeping in memory the entire  $N^3$  DNS,  $N$  being the resolution, is too demanding in storage memory. To reduce the volume of the dataset without losing the properties of the different modes, only the six planes:  $k_x = \{0; 1\}$ ,  $k_y = \{0; 1\}$  and  $k_z = \{0; 1\}$  are outputted for the  $TG$  symmetric TYGRE code and only the three planes:  $k_x = 0$ ,  $k_y = 0$  and  $k_z = 0$  are outputted for the general-periodic GHOST code. The velocity time series are then multiplied by an apodization function [29] and Fourier-transformed to form a dataset in the  $\mathbf{k} - \omega$  space. The power spectrum  $s(\mathbf{k}, \omega)$  is then computed by taking the modulus square of the velocity and summing over the different Cartesian directions. The isotropic power spectrum  $S(k, \omega)$  is computed by summing the power spectrum over the modes of same wavenumber. A binning of spacing of one is used to compute the isotropic power spectrum. The closest integer smaller than  $k + \frac{1}{2}$  is used to define the bin number. The left panel of fig. 4 represents the power spectrum of a truncated Euler DNS computed using this method. The correlation function  $\Gamma(k, t)$  is then computed using Wiener-Khinchin theorem by performing a Fourier-transform of the isotropic power spectrum and normalizing the function. The right panel of fig. 4 represents the correlation function of a truncated Euler DNS computed using this method.

Finally, the correlation time can be computed by doing a fit of the correlation function in a well-resolved domain as shown in the left panel of fig. 5. The time where the correlation function reaches half-height,  $\tau_{\frac{1}{2}}$ , can be evaluated numerically. The same algorithm can be used to find the correlation function of the positive and negative helical modes of the velocity field using eq. (10). The steps of the procedure are summed up in the algorithm presented below.

---

**Require:**  $\mathbf{u}(\mathbf{k}, n\Delta t)$ ,  $n$ ,  $\Delta t$ ,

- 1:  $\mathbf{u}(\mathbf{k}, \omega) = D\mathcal{F}[apo(n, \Delta t)\mathbf{u}(\mathbf{k}, n\Delta t)](\omega)$
  - 2:  $s(\mathbf{k}, \omega) = \sum_i |\mathbf{u}_i(\mathbf{k}, \omega)|^2$
  - 3:  $S(k, \omega) = \sum_{\mathbf{k}} \mathbf{1}_k s(\mathbf{k}, \omega)$
  - 4:  $\gamma(k, t) = D\mathcal{F}^{-1}[S(k, \omega)](t)$
  - 5:  $\Gamma(k, t) = \gamma(k, t)/\gamma(k, 0)$
  - 6:  $\tau(k) = Solve[t, \Gamma(k, t), 1/2]$
- 

Algorithm to compute the correlation time.  $D\mathcal{F}$  denotes the discrete Fourier-transform,  $D\mathcal{F}^{-1}$  denotes the discrete inverse Fourier-transform,  $\mathbf{1}$  denotes the characteristic function satisfying  $\mathbf{1}(bool) = 1$  if  $(k - \frac{1}{2} < |\mathbf{k}| \leq k + \frac{1}{2})$  and 0 otherwise,  $apo(n, \Delta t)$  denotes an apodization function and  $Solve[t, \Gamma(k, t), 1/2]$  denotes a function that finds the smallest positive  $t$  satisfying  $\Gamma(k, t) = 1/2$ .

- 
- [1] F. H. Champagne, “The fine-scale structure of the turbulent velocity field,” *Journal of Fluid Mechanics* **86**, 67–108 (1978).
  - [2] Yukio Kaneda, Takashi Ishihara, Mitsuo Yokokawa, Kenichi Itakura, and Atsuya Uno, “Energy dissipation rate and energy spectrum in high resolution direct numerical simulations of turbulence in a periodic box,” *Physics of Fluids* **15**, L21–L24 (2003).
  - [3] Uriel Frisch, *Turbulence: the legacy of AN Kolmogorov* (AIP, 1996).
  - [4] Andrei N. Kolmogorov, “The local structure of turbulence in incompressible viscous fluid for very large Reynolds numbers,” in *Dokl. Akad. Nauk SSSR*, Vol. 30 (JSTOR, 1941) pp. 301–305.
  - [5] Dieter Forster, David R. Nelson, and Michael J. Stephen, “Large-distance and long-time properties of a randomly stirred fluid,” *Physical Review A* **16**, 732–749 (1977).
  - [6] Robert H. Kraichnan and Shiyi Chen, “Is there a statistical mechanics of turbulence?” *Physica D: Nonlinear Phenomena* **37**, 160–172 (1989).
  - [7] Robert H. Kraichnan, “Helical turbulence and absolute equilibrium,” *JFM* **59**, 745–752 (1973).
  - [8] Cyril Cichowlas, Pauline Bonati, Fabrice Debbasch, and Marc Brachet, “Effective Dissipation and Turbulence in Spectrally Truncated Euler Flows,” *Physical Review Letters* **95**, 264502 (2005).
  - [9] G. Krstulovic, P. D. Mininni, M. E. Brachet, and A. Pouquet, “Cascades, thermalization, and eddy viscosity in helical Galerkin truncated Euler flows,” *Physical Review E* **79**, 056304 (2009).
  - [10] V. Dallas, S. Fauve, and A. Alexakis, “Statistical Equilibria of Large Scales in Dissipative Hydrodynamic Turbulence,” *Physical Review Letters* **115**, 204501 (2015).
  - [11] U Frisch, Zh S She, and PL Sulem, “Large-scale flow driven by the anisotropic kinetic alpha effect,” *Physica D: Nonlinear Phenomena* **28**, 382–392 (1987).
  - [12] Alexandre Cameron, Alexandros Alexakis, and Marc-Etienne Brachet, “Large-scale instabilities of helical flows,” *Physical Review Fluids* **1**, 063601 (2016).
  - [13] T. D. Lee, “On some statistical properties of hydrodynamical and magneto-hydrodynamical fields,” *Quarterly of Applied Mathematics* **10**, 69–74 (1952).
  - [14] L. D. Landau and E. M. Lifshitz, *Statistical Physics* (Butterworth-Heinemann, Burlington, 1980).
  - [15] Antoine Craya, *Contribution a l’analyse de la turbulence associee a des vitesses moyennes*, Thesis, Universite de Grenoble (1957).
  - [16] J.R. Herring, “Approach of axisymmetric turbulence to isotropy,” *The Physics of Fluids* **17**, 859–872 (1974).
  - [17] Marc E. Brachet, Daniel I. Meiron, Steven A. Orszag, B. G. Nickel, Rudolf H. Morf, and Uriel Frisch, “Small-scale structure of the Taylor-Green vortex,” *Journal of Fluid Mechanics* **130**, 411–452 (1983).
  - [18] A. Pouquet, E. Lee, M. E. Brachet, P. D. Mininni, and D. Rosenberg, “The dynamics of unforced turbulence at high Reynolds number for TaylorGreen vortices generalized to MHD,” *Geophysical & Astrophysical Fluid Dynamics* **104**, 115–134 (2010).
  - [19] P. D. Mininni, A. Alexakis, and A. Pouquet, “Nonlocal interactions in hydrodynamic turbulence at high Reynolds numbers: The slow emergence of scaling laws,” *Physical review E* **77**, 036306 (2008).
  - [20] Pablo D. Mininni, Duane Rosenberg, Raghu Reddy, and Annick Pouquet, “A hybrid MPIOpenMP scheme for scalable parallel pseudospectral computations for fluid turbulence,” *Parallel Computing* **37**, 316–326 (2011).
  - [21] Caroline Nore, Malek Abid, and M. E. Brachet, “Decaying Kolmogorov turbulence in a model of superflow,” *Physics of Fluids* **9**, 2644–2669 (1997).
  - [22] Eric W. Weisstein, *Chi-Squared distribution* (Math\World - A Wol\fram Web Resource, 2017).
  - [23] Pablo Javier Cobelli, Agnes Maurel, Vincent Pagneux, and Philippe Petitjeans, “Global measurement of water waves by Fourier transform profilometry,” *Experiments in Fluids* **46**, 1037 (2009).
  - [24] Benjamin Miquel, Alexandros Alexakis, and Nicolas Mordant, “Role of dissipation in flexural wave turbulence: From experimental spectrum to Kolmogorov-Zakharov spectrum,” *Physical Review E* **89**, 062925 (2014).
  - [25] P. Clark di Leoni, P. J. Cobelli, and P. D. Mininni, “The spatio-temporal spectrum of turbulent flows,” *The European Physical Journal E* **38**, 136 (2015).
  - [26] Eric W. Weisstein, *Wiener-Khinchin Theorem* (MathWorld - A Wolfram Web Resource, 2017).
  - [27] Thierry Dombre, Uriel Frisch, John M. Greene, Michel Henon, A. Mehr, and Andrew M. Soward, “Chaotic streamlines in the ABC flows,” *Journal of Fluid Mechanics* **167**, 353–391 (1986).
  - [28] Alexandre Cameron and Alexandros Alexakis, “Fate of Alpha Dynamos at Large Rm,”

Physical Review Letters **117**, 205101 (2016).

[29] Eric W. Weisstein, *Apodization Function* (MathWorld - A Wolfram Web Resource, 2017).